Apparent splitting of S waves propagating through an isotropic lowermost mantle

Laura Parisi [1,2], **Ana M. G. Ferreira** [3,4] **and Jeroen Ritsema** [5]

[1]PSE Division, King Abdullah University of Science and Technology, Thuwal, Saudi Arabia.
[2]School of Environmental Sciences, University of East Anglia, Norwich, UK.
[3]Department of Earth Sciences, University College of London, London, UK.
[4]CEris, ICIST, Instituto Superior Técnico, Universidade de Lisboa, 1049-001 Lisboa, Portugal.
[5]Department of Earth and Environmental Sciences, University of Michigan, Ann Arbor, Michigan, USA.

Key Points:

- Simulations of wave propagation through the lowermost mantle display apparent SH-SV splitting for 1-D and 3-D isotropic Earth models.
- The apparent splitting is due to phase interference between S and reflected waves.
- Anomalous Vs gradients, discontinuities, and heterogeneities may lead to misinterpretation of wave splitting.

This is the author manuscript accepted for publication and has undergone full peer review but has not been through the copyediting, typesetting, pagination and proofreading process, which may lead to differences between this version and the Version of Record. Please cite this article as doi: 10.1002/2017JB014394

Corresponding author: Laura Parisi, `laura.parisi@kaust.edu.sa`

Abstract

Observations of shear-wave anisotropy are key for understanding the mineralogical structure and flow in the mantle. Several researchers have reported the presence of seismic anisotropy in the lowermost 150–250 km of the mantle (i.e., D” layer), based on differences in the arrival times of vertically (SV) and horizontally (SH) polarized shear waves. By computing waveforms at period > 6 s for a wide range of 1-D and 3-D Earth structures we illustrate that a time shift (i.e., apparent splitting) between SV and SH may appear in purely isotropic simulations. This may be misinterpreted as shear wave anisotropy. For near-surface earthquakes, apparent shear wave splitting can result from the interference of S with the surface reflection sS. For deep earthquakes, apparent splitting can be due to the S-wave triplication in D”, reflections off discontinuities in the upper mantle and 3-D heterogeneity. The wave effects due to anomalous isotropic structure may not be easily distinguished from purely anisotropic effects if the analysis does not involve full waveform simulations.

1 Introduction

The D” layer — the lowermost 150–250 km of the mantle [*Bullen*, 1950]— plays a key role in global dynamics (for a recent review see, e.g., *Lay* [2015]). D” is heterogeneous at various scales. It is characterized by anomalous radial wave speed gradients [e.g., *Young and Lay*, 1987a], a seismic discontinuity at its top [e.g., *Lay and Helmberger*, 1983; *Wysession et al.*, 1998], large low shear velocity provinces (LLSVPs) [e.g., *Lekic et al.*, 2012; *Garnero et al.*, 2016], ultra low velocity zones [e.g., *Garnero et al.*, 1993; *Cottaar and Romanowicz*, 2012; *Thorne et al.*, 2013], and anisotropic shear wave speed structure [e.g., *Meade et al.*, 1995; *Montagner and Kennett*, 1996; *Nowacki et al.*, 2011].

The presence of shear wave anisotropy, in particular, is important for interpreting the mineralogy and deformation of the D” layer. Seismic anisotropy could be due to lattice-preferred orientation (LPO) of minerals [e.g., *McNamara et al.*, 2002] such as post-perovskite [e.g., *Murakami et al.*, 2004; *Oganov et al.*, 2005; *Iitaka et al.*, 2004] or shape preferred orientation (SPO) involving structural elements, such as layers of melt [e.g., *Kendall and Silver*, 1996]. Possibly, deformation of ancient slabs which have subducted into the lowermost mantle may be responsible for the anisotropy [e.g., *McNamara et al.*, 2002].

Seismic anisotropy in D" is quantified by the difference in the arrival times or phase shifts of vertically (SV) and horizontally (SH) polarized shear wave phases (i.e., shear wave splitting) such as S, ScS, and Sdiff. Shear-wave splitting up to 5 s, as reported in numerous studies, correspond to radial anisotropy $\xi = V_{SH}^2/V_{SV}^2$ up to 1.06, depending on epicentral distance (Figure S1 in the supplementary information). Most observations of anisotropy suggest that V_{SH} is higher than V_{SV} in regions of D" where the shear velocity is relatively high (see *Nowacki et al.* [2011] for a recent review). These include the D" region beneath Alaska [e.g., *Garnero and Lay*, 1997; *Wysession et al.*, 1999], the Caribbean [*Kendall and Silver*, 1996], the Indian Ocean [*Ritsema*, 2000], and Siberia [*Thomas and Kendall*, 2002]. The pattern of anisotropy is more complex within the LLSVPs and the transition zones between LLSVPs and the high-velocity regions of D". Here, shear wave anisotropy is weak and recordings for similar source-receiver paths provide evidence for $V_{SV} < V_{SH}$ and $V_{SV} > V_{SH}$ and azimuthal variations [e.g., *Vinnik et al.*, 1995, 1998; *Pulliam and Sen*, 1998; *Ritsema et al.*, 1998; *Kendall and Silver*, 1998; *Fouch et al.*, 2001; *Garnero et al.*, 2004].

It is not straightforward to interpret shear wave splitting and to construct models of anisotropy. Recent studies have shown that it is difficult to constrain D" anisotropy using global tomographic inversions because S waves traveling in D" are mostly sensitive to V_{SH}. The unbalanced sensitivity to V_{SH} and V_{SV} results in leakage of heterogeneity into artificial anisotropic structure in D" [e.g., *Kustowski et al.*, 2008; *Chang et al.*, 2014, 2015]. Moreover, measuring shear wave splitting can be difficult because teleseismic S waves have low amplitudes after they have diffracted around the core [e.g. *Doornbos and Mondt*, 1979]. Core-diffraction and the interference with reflections off the core or layers within D" affect SV and SH differently. Here we refer to the traveltime difference between SH and SV waves as "apparent splitting" when it is not due to seismic anisotropy.

The forward modeling tests by *Maupin* [1994], *Komatitsch et al.* [2010], and *Borgeaud et al.* [2016] demonstrate that the traveltimes of diffracted SH and SV waves can be different, even when the lowermost mantle has an isotropic shear wave structure. *Maupin* [1994] showed that the traveltime difference between SH and SV waves is not a discriminating factor between isotropic and anisotropic D" models. She argued that particle motion can be used to constrain azimuthal anisotropy. *Komatitsch et al.* [2010] used spectral-element method simulations for an earthquake at the Earth's surface to argue that the splitting between SHdiff and SVdiff can be as high as 15 s for 1-D isotropic Earth models. *Borgeaud et al.* [2016] investigated the bias introduced by ray-theory in the measurement of splitting in S waves travelling through the lowermost mantle and argued that SH and SV traveltimes can differ by as much as 16 s for 1-D Earth models based on mineral physics and geodynamical information.

In this work, we expand on previous studies by investigating the effect of the earthquake source depth on waveforms and by exploring apparent splitting for a wide range of 1-D and 3-D isotropic structures for waveforms at periods longer than about 6 s. We study how wave interference affects the waveforms of SH and SV that propagate through D", notably by analyzing S-sS interference for shallow earthquakes and the S wave triplication at the top of D" for deep earthquakes. We quantify apparent splitting for a large number of shear velocity models built by systematically: (i) varying the thickness and radial shear velocity gradient in D"; (ii) considering a shear velocity discontinuity at the top of D"; and, (iii) including large-scale 3-D shear velocity variations in the mantle.

2 Full waveform simulations of deep mantle shear waves

We compute synthetic seismograms using Gemini (GEM) [*Friederich and Dalkolmo*, 1995] and the spectral element method (SEM) [e.g., *Komatitsch and Vilotte*, 1998]. Simulations based on 1-D Earth models are run with GEM and the simulations based on 3-D Earth models are run with SEM. GEM is based on a minor integration technique and enables fast accurate waveform calculations at high frequencies and for 1-D Earth models. GEM synthetics are calculated on a single processor core at maximum frequency of 200 mHz. GEM calculations use spherical harmonics up to 5000 degree with a step of 1. On the other hand, SEM allows for the computation of waveform propagation through fully 3-D Earth models [e.g., *Komatitsch and Tromp*, 2002a; *Parisi et al.*, 2015; *Parisi and Ferreira*, 2016] but the simulations at short periods rely on fine meshes and relatively small time steps. We use the SPECFEM3D_GLOBE package [e.g., *Komatitsch and Tromp*, 2002a,b] adapted for simulations to wave periods as short as 5.6 s and run simulations on 3,456 processor cores by splitting the mesh into 24×24 slices for each of the 6 chunks in which the globe is subdivided. The number of the elements at the surface of each chunk is set to 768×768. The length of the seismograms obtained from GEM and SEM simulations is 33 minutes.

We estimate time shifts (i.e., splitting) between SV and SH by manually identifying SH and SV onsets (t$_{SV} - t_{SH}$). For completeness, we also measure t$_{SV} - t_{SH}$ by using a cross-correlation approach. Although cross–correlation measurements are more objective, they may be problematic in cases of waveform dissimilarity and differences in frequency content [*Borgeaud et al.*, 2016]. Overall, our splitting measurements obtained by cross-correlation and from onsets are consistent when the cross-correlation between the SH and SV waveforms is higher than 0.85 (see Figure S2 in the supplementary information). Throughout this manuscript we discuss results based on onset measurements when the S phase onset can be clearly identified and there is good similarity between the SH and SV waveforms. Onset picks are not shown for sets of waveforms calculated with an Earth's model for which apparent splitting is not observed.

3 Apparent splitting for a shallow earthquake source

3.1 Method's validation

Since SPECFEM3D_GLOBE has not been extensively tested at periods as short as T ~ 6 s, we first validate our calculations by reproducing some of the results of *Komatitsch et al.* [2010] using both SEM and GEM. Waveforms are calculated for a near-vertical dip-slip earthquake (strike=0°, dip=20°, rake=45°) at the Earth's surface (depth = 0.1 km) at epicentral distances between 90° and 120°. As in *Komatitsch et al.* [2010], the seismic model is a simplified version of the IASP91 profile [*Kennett and Engdahl*, 1991, Figure 1]. There is no shear attenuation, the crust is removed and the discontinuities in the upper mantle have been replaced by strong gradients (Figure 1b).

The waveforms are convolved with a Gaussian source time function with a half-duration of 6.5 s and filtered using a 6th order Butterworth bandpass filter with corners at 7 s and 80 s. Figure 2 replicates the results of *Komatitsch et al.* [2010, their Figure 3]. Our SEM and GEM simulations are equivalent. Minor differences in the radial components are visible at distance larger than 116° because SV amplitudes decrease strongly at distances larger than about 95° due to diffraction around the core. Even though the Earth model is isotropic, there is an apparent splitting between the SVdiff (on the radial component) and SHdiff waveforms (on the transverse component) that reaches 1.8 s at a distance of 120°. There are small differences in the splitting estimates between our and *Komatitsch*

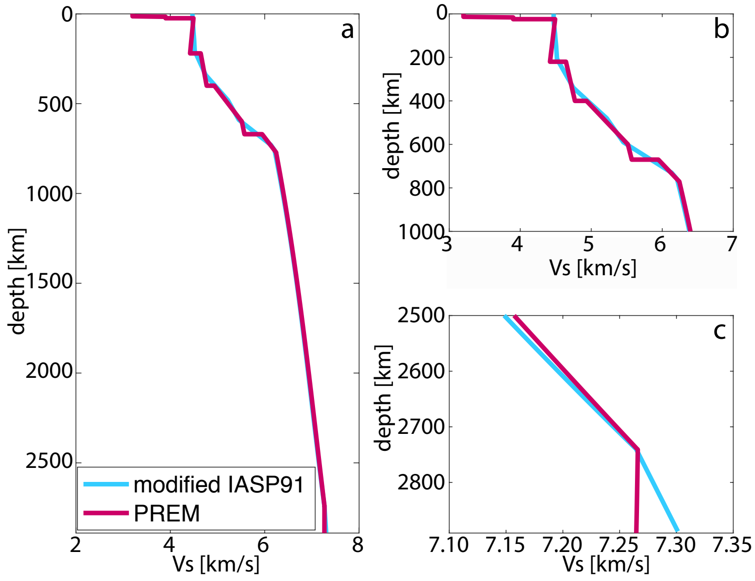

Figure 1. **a)** Vs crustal and mantle profiles for the modified version of the IASP91 model (in blue) and the PREM model (in purple). **b)** Zoom of a) in the top 1000 km of the mantle. **c)** Zoom of a) in the lowermost mantle.

et al. [2010]'s study probably because of the slightly different waveform processing. However, the apparent splitting is confirmed.

3.2 Effects of earthquake source depth

To investigate the cause of the apparent splitting observed in the previous experiment, we show in Figure 3 waveforms at a distance of 110° for the same dip-slip earthquake and the same source-receiver azimuth as in Figure 2, but for focal depths of 0.1, 10, 20, 30, 40 and 50 km. The marked arrival times of several high-amplitude phases are calculated using the TauP method [*Crotwell et al.*, 1999] for the modified IASP91 model shown in Figure 1.

In Figures 2 and 3 (at depth 0.1 km), the apparent splitting seems to be related to Sdiff with positive polarity, both on the radial and transverse components. From the waveforms at depths larger than 30 km, it is evident that sSHdiff has a positive polarity and SHdiff has a negative polarity on the transverse component. At a depth of 0.1 km when SHdiff and sSHdiff arrive simultaneously, the sum of the two signals has a positive polarity because sSHdiff is stronger than SHdiff. Figure S3 illustrates in detail how SHdiff

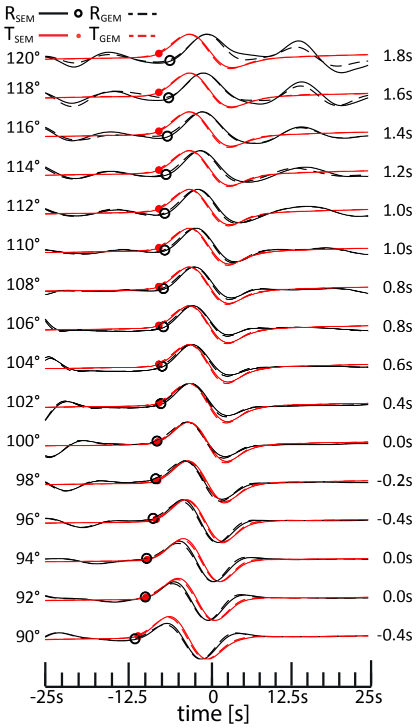

Figure 2. Comparisons between velocity waveforms calculated with SEM (solid lines) and GEM (dashed lines). The earthquake source is located at [lat,lon,depth] = [0°,0°,0.1 km] and has a focal mechanism with strike = 0°, dip = +20° and rake = +45°. The seismic stations are placed on the equator to the east (at azimuth of 90°) at epicentral distances reported on the left of the waveforms. SV (black circles) and SH (red dots) onsets are marked on the waveforms. The apparent SH-SV splitting is shown on the right of each pair of waveforms. Every waveform is normalized with respect to its own maximum amplitude. The time scale and reduction slowness (8.3 s/°) are as in *Komatitsch et al.* [2010]

emerges from sSHdiff with a negative onset as the source depth increases from 1 km to 5 km. The waveforms for source depths of 20 km and larger indicate that sSVdiff has a positive polarity and that SVdiff is very weak on the radial component. Therefore, the apparent splitting observed at depth of 0.1 km (as in *Komatitsch et al.* [2010]'s example) is due to a time shift between SHdiff+sSHdiff on the transverse component and sSVdiff on the radial component. The interference of Sdiff with sSdiff affects the radial and transverse components differently because sSVdiff is much weaker than sSHdiff. This suggests that the earthquake's focal mechanism can have a strong effect on the apparent splitting, which will be further investigated in future work. For completeness, Figure S4 presents results at an epicentral distance of 114 degrees, for which the apparent splitting for a source at 0.1

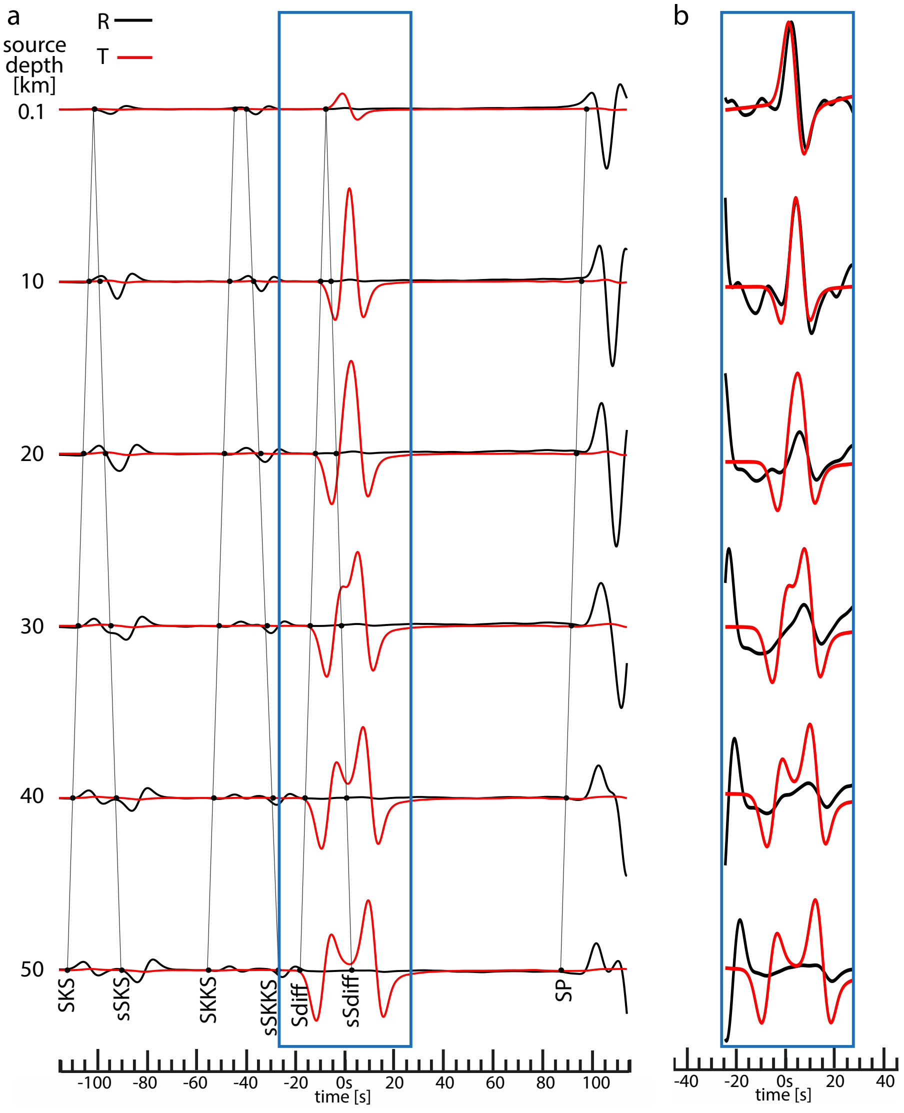

Figure 3. Effect of source depth on the differential arrival-times of some seismic phases. **a)** Velocity waveforms as in Figure 2 but for different source depths (reported on the left). The source mechanism and location are as in Figure 2 and all the waveforms are calculated at the epicentral distance of 110°. Each waveform is normalized with respect to its own maximum amplitude in each subplot. The time scale is the same for each subplot. Black lines show the theoretical onset arrival-times for the main seismic phases. **b)** Waveforms as in a) but normalized in the time window included in the blue box (same time window as in Figure 2). The waveforms are all filtered with a 6th order Butterworth low-pass filter with corner frequency 0.2 Hz.

km depth is larger than at 110 degrees (Figure 2). Similar to Figure 3, once the negative polarity of SHdiff starts to emerge (in this case, for a source depth of 2 km), the splitting reduces, because the SHdiff and sSHdiff phases start to separate.

4 Apparent splitting for a deep earthquake source

From here on, we compute seismic waveforms for deep earthquakes, which are typically used in shear-wave splitting studies. Specifically, we use the source-receiver path between the M_W 5.8, 30 August 1994, Banda Sea earthquake at a depth of 604 km (Figure 4) and stations in eastern Africa. For this normal faulting event, *Ritsema* [2000] measured SH-SV splitting of 1–3 s (with SH faster than SV) at stations from a temporary network in Tanzania at epicentral distance of 87–91°.

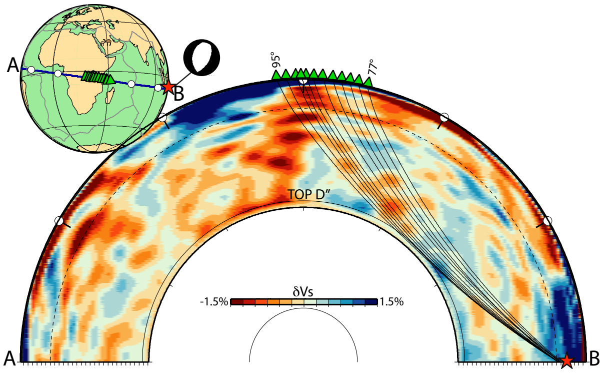

Figure 4. Source-receiver configuration for the 30 August 1994, deep (604 km), M_W 5.8 Banda Sea earthquake. The source location is represented by a red star and the focal mechanism is shown in the subplot on the top left of the figure. Receivers are represented by green triangles. The tomographic cross-section shows the Vs perturbations of the isotropic part of the SGLOBE-rani tomographic model with respect to the isotropic PREM model. Seismic rays connecting the source and receivers are calculated using PREM.

4.1 Effects of 1-D velocity structure in the D" layer

We systematically explore a range of isotropic models to investigate whether complexity in D" can lead to apparent splitting in the same order of magnitude as reported for many high–velocity and low–velocity regions in the D" layer. We assume the PREM attenuation structure and source parameters from the global CMT catalogue [*Dziewonski et al.*, 1981; *Ekström et al.*, 2012]. We convolve the synthetics with a Gaussian source time function with a half duration of 2.9 s (as reported in the CMT solution) and apply the same band-pass filter as before.

Figure 5 shows the fifteen 1-D isotropic Earth models for which we have synthesized waveforms. These models are based on the PREM model (mod1 in Figure 5) but the structure in D” has been modified to represent the wide variety of shear velocity profiles previously proposed for different regions of D”. Models mod2–mod6 have different radial shear velocity gradients in D” than in PREM. In mod2 the V_S gradient in D” layer is constant throughout the lowermost mantle. The shear velocity gradients in models mod3 and mod4 are $1.27 \times 10^{-4} s^{-1}$ and $-1.33 \times 10^{-4} s^{-1}$ in the lowermost 150 km of the mantle, respectively. The gradients in models mod5 and mod6 are $-11 \times 10^{-4} s^{-1}$ and $14 \times 10^{-4} s^{-1}$, respectively. Similar negative gradients are observed in recent 3-D global tomography models [e.g., *Chang et al.*, 2015] and 1-D profiles [*Ritsema et al.*, 1997] across the large low shear velocity provinces in D”. Models mod7–mod12 include velocity discontinuities at the top of D”. These velocity jumps range from 0.48% (in mod7) to 2.52% (in mod11). The strength of these velocity discontinuities is similar to that reported for downwelling regions [e.g., *Young and Lay*, 1987a,b; *Helmberger et al.*, 2005; *Yao et al.*, 2015; *Sun et al.*, 2016].

The waveforms are computed for stations from the Tanzania network and hypothetical stations along the source-receiver great-circle arc. As examples, waveforms for the models mod5, mod10 and mod14 are displayed in Figure 6. Figures S5–S7 (in the Supporting Information) show the waveforms calculated for all models in Figure 5.

We analyse the radial and transverse component waveforms computed for the fifteen models in Figure 5 and classify the waveforms as having: (i) no apparent SH-SV splitting nor wider pulses (models labeled as "no effects" in green in Figure 5); (ii) SH pulses wider than SV (models labeled as "wider SH" in orange in Figure 5); and, (iii) SH-SV apparent splitting (models labeled as "apparent SWS" in red in Figure 5). We find that models mod9–mod11 with strong velocity discontinuities lead to a clear apparent splitting while models mod4-mod6 and mod12-mod15, with low velocity in the lowermost mantle, cause a widening of the SH waveforms. The remaining models do not modify the SH and SV waveforms significantly.

For any realistic 1-D reference model, ScS and SKS are the two high-amplitude phases with similar arrival times to S between 77° and 95°. ScS arrives later than S and modifies the tail of the S wave at distances larger than about 80°. At distances shorter than about 81° SKS arrives earlier than S and can modify the S onset. The interference of S with ScS and SKS is different on the radial and transverse components. SKS is recorded

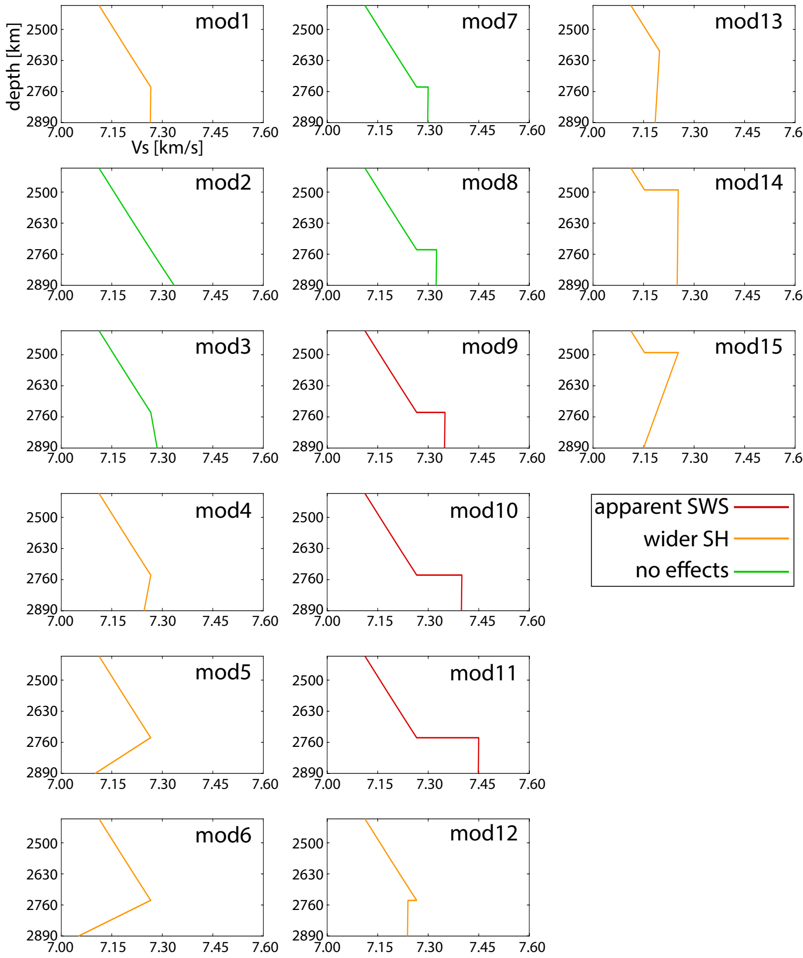

Figure 5. 1-D isotropic models of the lowermost mantle used to simulate waveforms for the Mw 5.8 Banda Sea earthquake. Shallower parts of the models, not included in the plots, are as in PREM (see Figure 1). Colour code of the velocity profiles is used to indicate cases in which either apparent splitting (red), or widening of the SH pulse (orange) or no effect on the waveforms (green) is observed in the corresponding theoretical waveforms.

only on the radial component and modifies the SV waveform only. ScS has the same polarity as S on the transverse component but opposite polarity on the radial component.

The interference of S with ScS depends also on the shear velocity structure. In the presence of a negative shear velocity gradient, S and ScS are more separated and the SH pulse is wider than in PREM. The SH pulse is particularly wide for models mod4 to mod6 in Figure 5. Waveforms for mod5 (Figure 6a) show that the SH pulse widening is evident at distances from 90° to 95° (stations PUGE, URAM, AA6 and AA7). At dis-

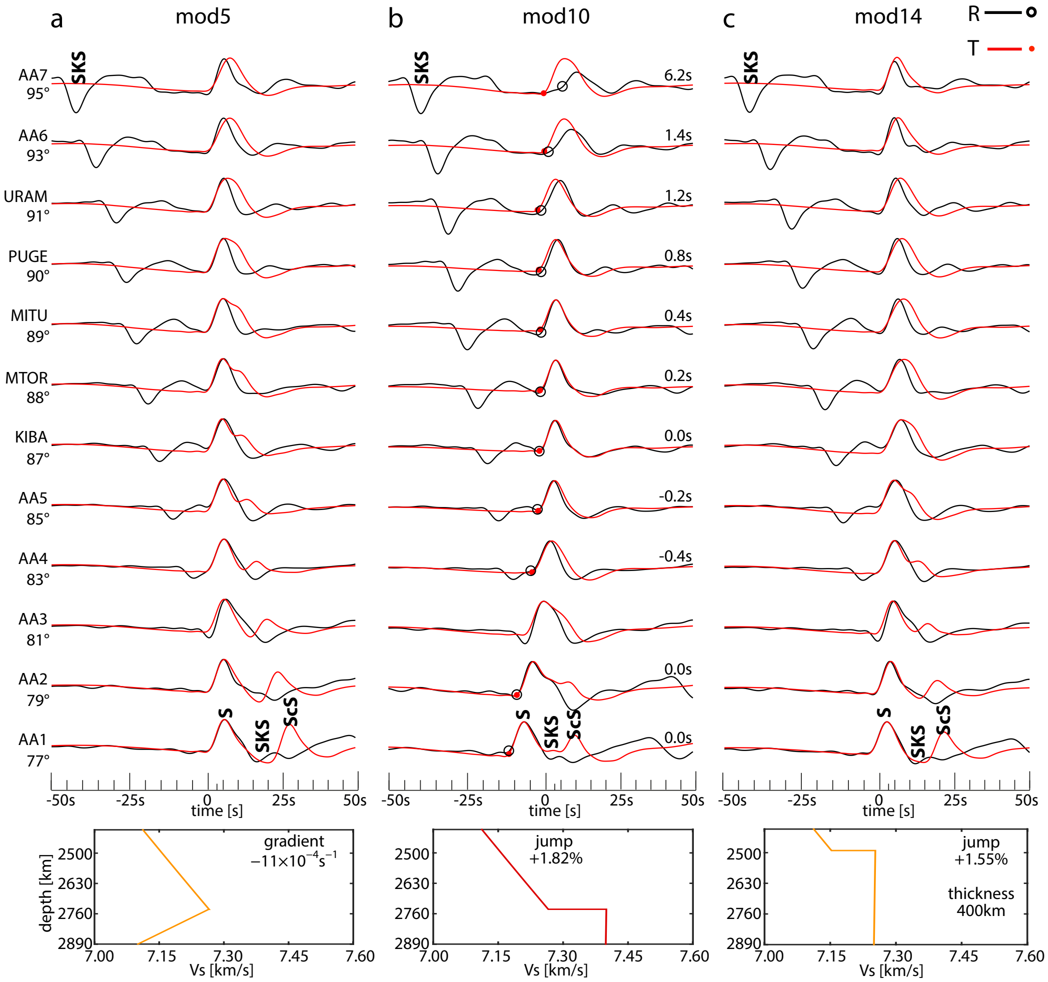

Figure 6. Examples of waveforms calculated for the Mw 5.8 Banda Sea earthquake. The source-receiver geometry is shown in Figure 4. The 1-D model used in the simulations is shown below each set of waveforms (see also Figure 5). On the left of the waveforms, the names of the stations and the epicentral distances are reported. Names of the seismic phases discussed in the text are reported. SV (black circles) and SH (red dots) onsets are marked on the waveforms. The apparent splitting is reported on the right of the waveforms. Every waveform is normalized with respect to its own maximum amplitude.

tances shorter than 90° when S and ScS are separated by more than 4–5 s, the SH waveforms are double peaked (stations AA5, KIBA, MTOR, MITU).

The interference of S with ScS for models with a shear velocity discontinuity at the top of D” larger than 1.14% (models from mod9 to mod11) generates apparent splitting. The D” discontinuity causes, in fact, an S wave triplication comprising a direct S wave (Sab), a S wave turning below the discontinuity (Scd), and a S wave reflecting off the discontinutiy (Sbc). Their relative arrival times depend on the epicentral distance and velocity jump. For mod10 (Figure 6b), Sab arrives before Scd at distances shorter than 85° and the interference of the triplicated S and ScS results in a widening of SH. Between 85° and 87°, Scd arrives before Sab and the interference results in a negative apparent splitting. At epicentral distances larger than 88°, ScS arrives within the triplication and the interference results in a positive apparent splitting growing with the epicentral distance. At epicentral distances larger than 91°, Sbc and Sab are no longer recorded. Although we measure large apparent splitting at these epicentral distances, the large difference in the waveforms prevent us from making further interpretations.

The range of epicentral distances where the interference between the triplicated S and ScS depends non-linearly on the depth and on the amplitude of the Vs jump at the top of the D” layer. For example, despite the strong velocity jump, models mod14 and mod15 only produce a widening of the SH pulse – and no apparent splitting – in the range of epicentral distances analysed (Figure 6c) because the layer is thick compared to models mod9–mod11.

The apparent shear wave splitting values measured for models mod9–mod11 are summarized in Figure 7a. We find small, negative shear wave splitting values (i.e., SV faster than SH) for most models of Figure 7a for the shortest (< 88°) epicentral distances. The largest, positive splitting values (up to ~7.2 s) are seen at the largest distances. Overall, the range of shear wave splitting values measured in our synthetics is on the same order as measurements from real data reported in the literature (Figure 7b).

5 Effects of 3-D velocity structure on the apparent splitting

To understand whether 3-D velocity heterogeneity can complicate further the interpretation of shear wave splitting, we repeat some of the experiments described in sections 3 and 4 by incorporating 3-D global tomographic models in the full waveform modelling simulations using SEM.

5.1 Deep dip-slip source model

Figure 8 shows waveforms for the same dip-slip source model used in section 3, but now for a source depth of 604 km, since shear wave splitting studies are typically based on deep earthquake data. We use two different 3-D isotropic Earth models that include

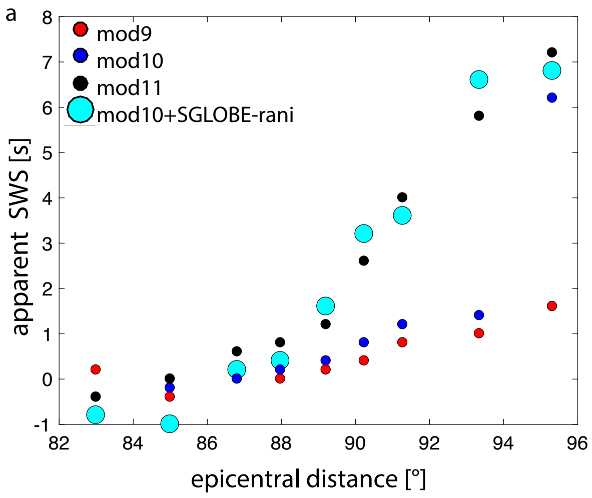

b

	Distance	SWS
South East Pacific	~90°	~-2s -- ~+2s
Ford at al., 2006	~95°	~-4s -- ~+4s
Caribbean	~90°	~+2s
Kendall and Silver, 1996	~92°	~+5s
Alaska	~90°	0 -- ~+1.5s

Figure 7. a) Scatter plot of apparent shear wave splitting (SWS) values measured in this study against the epicentral distance. Small circles denote the 1-D isotropic models with a Vs jump at the D” discontinuity (mod9, mod10 and mod11, shown in Figure 5) for which apparent splitting is observed. Large circles denote the apparent splitting observed for the 3-D model superimposing the isotropic part of SGLOBE-rani on mod10. b) Illustrative observed values of SH-SV splitting from the literature for various D” regions are reported for comparison.

the global crustal model CRUST2.0 [*Bassin et al.*, 2000], the PREM attenuation and two whole mantle models: (i) S40RTS [*Ritsema et al.*, 2011]; and, (ii) the isotropic part of the more recent SGLOBE-rani model [*Chang et al.*, 2015]. Both 3-D Earth models are defined as Vs perturbations with respect to the reference model PREM and in our calculations we use an isotropic version of PREM (i.e., excluding PREM’s upper mantle anisotropy). We also calculate reference waveforms for PREM to highlight the effects of the 3-D Earth structure in the waveform analysis. Figure 8 shows waveforms simulated at azimuths of 90° and 270°.

Figures 8c and 8f show that the waveforms and the apparent splitting values obtained for PREM are different for the two azimuths. Apparent splitting ranges from 0.8 s to 3.4 s at an azimuth of 90° and from -0.6 s to -0.2 s at an azimuth of 270°. At an azimuth of 90°, a strong arrival on the radial component interferes with SV at a distance of 90° and moves out with distance. This signal arrives about 20 s after S at 96°. Travel-time calculations show that this strong arrival is consistent with the arrival time of S^220P, the S wave reflected off under the 220-km mantle discontinuity. The interference between S and S^220P has a minor effect on the waveforms at azimuth of 270° because of the higher amplitude ratio between S and S^220P. Thus, the difference in waveforms and apparent splitting observed at the two azimuths is due to the focal mechanism used in this experiment that radiates seismic energy differently along the two azimuths analysed.

For an azimuth of 90°, the S wave modelled in the 3-D Earth models (Figures 8d-e) traverses the large-low shear velocity province beneath Africa just before traveling through the D” region (Figure 8a). Moreover, the S wave travelling at distances larger than 102° crosses a high-velocity anomaly in the uppermost ~500 km of the mantle, before reaching the surface. Due to this shallow high-velocity anomaly the S^220P arrives earlier than in the 1-D model PREM. The different interference features in the two 3-D Earth models cause different apparent splitting values.

For an azimuth of 270°, the S wave in the 3-D Earth models (Figures 8g-h) crosses a low-velocity mantle before travelling through D”. S waves travelling at distance larger than 104° also cross the high-velocity anomaly of the South-America slab between the D” and the Earth’s surface (Figure 8b). Waveforms and splitting for the two 3-D Earth models are different from the corresponding ones calculated with the 1-D model and there are only two clear cases of observed splitting for the 3-D mantle model SGLOBE-rani (Figure 8g) at epicentral distances of 102° and 104°, where S is clearly diffracted. *Borgeaud et al.* [2016] attributed the Sdiff wave apparent splitting to the different sensitivity of SV and SH to the core-mantle boundary (CMB). In our study, the differences in Vs structure near the CMB of the two 3-D Earth models compared to the PREM model lead to distinct CMB conditions and thus possibly to the observed differences in waveforms and shear splitting values of the diffracted waves.

5.2 The 1994 Mw 5.8 Banda Sea earthquake

In this section we use the same earthquake mechanism as in section 4 for the August 30, 1994, deep (604 km depth), Mw 5.8 Banda Sea earthquake. We superimpose the isotropic part of the global model SGLOBE-rani [*Chang et al.*, 2015] on the 1-D model mod10 (see Figures 5 and 6), so that the 3-D model includes a seismic velocity discontinuity at the top of D”. The mantle model is coupled with the global crustal model CRUST2.0 [*Bassin et al.*, 2000] and PREM attenuation. The S wave crosses a succession of weak positive and negative velocity anomalies as it travels from the earthquake source to the D”. On the other hand, from the D” to the surface, S traverses an average slow region, notably for the longest paths (see Figure 4).

Waveforms for this simulation are shown in Figure 9 together with the corresponding apparent splitting. The waveforms differ from the 1-D simulation for mod10. The apparent splitting is as strong as that obtained for mod11 (see Figure 7a), which has a D” discontinuity stronger than mod10. 3-D heterogeneity changes the ScS onsets compared to the 1-D simulation and hence modifies its interference with the S phase. This can be seen in almost all the epicentral distances when comparing the waveforms for mod10 and for mod10+SGLOBE-rani (Figures 6b and 9). Thus, the differences in apparent splitting between the 1-D and 3-D simulations are likely due to a distinct interference between the ScS and the triplicated S phase in the two types of simulations.

6 Discussion and conclusions

Using 1-D and 3-D waveform simulations, we have demonstrated that phase interference can distort SH and SV waveforms and cause apparent splitting between SH and SV waveforms even in an isotropic mantle. The characteristics of interference and the magnitude of the shear-wave splitting depend on the depth of the earthquake, seismic radiation pattern, D” thickness, Vs discontinuities and gradients, and 3-D Earth structure. The apparent splitting values obtained in this study are in the same order of magnitude as those reported in observational studies of shear wave splitting based on real data, which are often interpreted in terms of D” anisotropy.

We have found that in most of the cases apparent splitting is due to the anomalous interference of the direct S phase with other seismic phases. For near-surface earthquakes, notably for the source-receiver configuration used by *Komatitsch et al.* [2010], and epicentral distances ranging from 102° to 120° the interference of Sdiff with sSdiff can produce splitting up to 1.8 s. For deeper earthquakes, when S does not interfere with sS, apparent splitting may be due to the interference of a triplicated S with ScS or of S with a precursor of SP due to an upper mantle reflection for a favourable radiation pattern. Strong negative Vs gradients in the D" layer delay the onset of diffraction. Consequently, the separation of S and ScS broadens the SH waveform or produces a double-peak shape at the shortest distances and a SH pulse wider than SV at the longest distances. If a strong discontinuity (> 1.14%) is located at the top of the D", the interference of S triplicated at the discontinuity and ScS may lead to apparent splitting up to 7 s depending on the strength of the discontinuity and epicentral distance.

We also found that 3-D Earth structure can modify the waveforms and enhance or reduce the apparent splitting. In fact, seismic heterogeneity affects not only the arrival time and waveform of the waves interfering with the direct S, but also the epicentral distance at which S starts to diffract along the core–mantle boundary.

Positive shear wave splitting ($V_{SH} > V_{SV}$) has been detected in several high D" shear velocity regions underlying present or past subduction zones, such as beneath the Caribbean, Alaska, and N. Siberia [e.g., *Garnero and Lay*, 1997; *Kendall and Silver*, 1996; *Thomas and Kendall*, 2002]. Thus, many studies attribute it to positive D" radial anisotropy due to slab deformation and/or the collision of slabs with the CMB. Slab deformation can produce laminated structures or lattice-preferred orientation (LPO) in constituent minerals, which could be compatible with radial anisotropy [e.g., *McNamara et al.*, 2002]. However, our results indicate that such geodynamic interpretations must be made cautiously, as other factors such as Vs discontinuities at the top of D" can potentially produce similar apparent splitting.

This study follows previous studies that highlighted the possibility of apparent S splitting in D". In early work, Maupin (1994) used approximate forward modeling schemes to show that the distinction between the effects of isotropic and anisotropic structure on the Sdiff waveforms is not trivial. *Komatitsch et al.* [2010] used the spectral element method to demonstrate that apparent splitting of Sdiff waves can occur for 1-D Earth models. However, *Komatitsch et al.* [2010] considered an earthquake source very close to the surface and here we showed that the resulting apparent Sdiff splitting is due to interference of Sdiff and sSdiff for such a shallow source. Thus, in our simulations we also considered more realistic deep earthquake sources, which are typically used in real data studies to reduce such phase interference effects. *Borgeaud et al.* [2016] studied the apparent splitting of S due to finite-frequency effects and attributed the Sdiff apparent splitting to the different sensitivity of SV and SH to the boundary conditions between the solid mantle and liquid outer core. In particular, they highlighted that apparent shear wave splitting can result from the misidentification of triplicated phases, which is compatible with our results. In addition, *Kawai and Geller* [2010] showed that the resolution of the velocity of SV shear waves very close to the CMB is inherently limited due to the boundary condition of zero tangential traction at the CMB. In this work we confirm the apparent splitting reported by these previous studies and we emphasise phase interference as being a key cause of apparent splitting. Moreover, our study also complements previous work by showing that 3-D Earth structure can either enhance or reduce apparent splitting, depending on the region through which the waves propagate, which adds complexity to the shear wave splitting analysis. Nevertheless, we highlight that in the case of S waves diffracted along the core, phase interference and different sensitivity to the core-mantle boundary can both cause apparent splitting.

In conclusion, we systematically quantified apparent shear wave splitting for several source depths and for a wide range of Earth models, including anomalous Vs gradients, D” thickness, discontinuities and 3-D heterogeneity. Our analysis highlighted a strong interplay between the various source and structure parameters considered, which may lead to a misinterpretation of the splitting and potentially erroneous constraints on intrinsic D” anisotropy. Full waveform modelling considering realistic sources and a wide range of 1-D and 3-D Earth models as in this study is a promising way to address these issues. While the illustrative examples based on the global smooth 3-D Earth models used in this study are a useful first step to quantify their effect on apparent shear wave splitting, future efforts will be directed towards comprehensive 3-D full wavefield analyses including more complex D” structures and multiple source-receiver orientations.

Acknowledgments

Waveforms simulations are available to the reviewers in this repository

https://drive.google.com/drive/folders/0B1zZpyGk7o6GUnlZZEhNR1V3RVU?usp=sharing.

If the manuscript is accepted for publication, the waveforms will be available in the eQuake-RC platform (http://equake-rc.info/). We thank the two anonymous reviewers and the associatededitor for helpful comments. This research was carried out on the High Performance Computing Cluster supported by the Research and Specialist Computing Support services at the University of East Anglia and on Archer, the UK's National Supercomputing Service. We thank Andy Nowacki, James Wookey and the CoMITAC project for providing us with the version of SPECFEM3D_GLOBE modified for short–period simulations (funded by the European Research Council under the European Union's Seventh Framework Programme (FP7/2007-2013) / ERC Grant agreement 240473) and for fruitful discussions. Some figures were built using Generic Mapping Tools (GMT; Wessel & Smith 1998). This work also benefited from funding by the European Commission's Initial Training Network project QUEST (contract FP7-PEOPLE-ITN-2008-238007, http://www.quest-itn.org) and discussions offered by the COST Action TIDES (http://www.tides-cost.eu/). AMGF and LP also thank funding from the Leverhulme Trust (project F/00 204/AS), followed by support from NERC project NE/K005669/1. In addition, AMGF also thanks support from NERC project NE/N011791/1. JR acknowledges support via NSF grant EAR-1565511.

References

Bassin, C., G. Laske, and G. Masters (2000), The current limits of resolution for surface wave tomography in North America, *EOS Trans. AGU*, *F897*, 81.

Borgeaud, A., K. Konishi, K. Kawai, and R. Geller (2016), Finite frequency effects on apparent S-wave splitting in the D" layer: Comparison between ray theory and full-wave synthetics, *Geophysical Journal International*, *207*(1), 12–28, doi:10.1093/gji/ggw254.

Bullen, K. E. (1950), An earth model based on a compressibility-pressure hypothesis, *Geophysical Journal International*, *6*.

Chang, S.-J., A. M. G. Ferreira, J. Ritsema, H. Van Heijst, and J. Woodhouse (2014), Global radially anisotropic mantle structure from multiple datasets: A review, current challenges, and outlook, *Tectonophysics*, *617*, 1–19, doi:10.1016/j.tecto.2014.01.033.

Chang, S.-J., A. M. G. Ferreira, J. Ritsema, H. J. van Heijst, and J. H. Woodhouse (2015), Joint inversion for global isotropic and radially anisotropic mantle structure including crustal thickness perturbations, *Journal of Geophysical Research: Solid Earth*, *120*(6), 4278–4300, doi:10.1002/2014JB011824.

Cottaar, S., and B. Romanowicz (2012), An unsually large ULVZ at the base of the mantle near Hawaii, *Earth and Planetary Science Letters*, *355-356*, 213–222, doi:

10.1016/j.epsl.2012.09.005.

Crotwell, H. P., T. J. Owens, and J. Ritsema (1999), The TauP Toolkit: Flexible seismic travel-time and ray-path utilities, *Seismological Research Letters*, *72*, 154–160.

Doornbos, D. J., and J. C. Mondt (1979), Attenuation of P and S waves diffracted around the core, *Geophysical Journal of the Royal Astronomical Society*, *57*(2), 353–379, doi: 10.1111/j.1365-246X.1979.tb04783.x.

Dziewonski, A., T.-A. Chou, and J. Woodhouse (1981), Determination of earthquake source parameters from waveform data for studies of global and regional seismicity, *Journal of Geophysical Research*, *86*(B4), 2825–2852.

Dziewonski, A. M., and D. L. Anderson (1981), Preliminary reference Earth model, *Physics of the Earth and Planetary Interiors*, *25*(4), 297–356.

Ekström, G., M. Nettles, and A. Dziewonski (2012), The global CMT project 2004-2010: Centroid-moment tensors for 13,017 earthquakes, *Physics of the Earth and Planetary Interiors*, *200–201*, 1–9, doi:10.1016/j.pepi.2012.04.002.

Fouch, M., K. Fischer, and M. Wysession (2001), Lowermost mantle anisotropy beneath the Pacific: Imaging the source of the Hawaiian plume, *Earth and Planetary Science Letters*, *190*(3-4), 167–180, doi:10.1016/S0012-821X(01)00380-6.

Friederich, W., and J. Dalkolmo (1995), Complete synthetic seismograms for a spherically symmetric Earth by a numerical computation of the Green's function in the frequency domain, *Geophysical Journal International*, *122*(2), 537–550.

Garnero, E., M. Moore, T. Lay, and M. Fouch (2004), Isotropy or weak vertical transverse isotropy in D" beneath the Atlantic Ocean, *Journal of Geophysical Research B: Solid Earth*, *109*(8), B08,308 1–10, doi:10.1029/2004JB003004.

Garnero, E., A. McNamara, and S.-H. Shim (2016), Continent-sized anomalous zones with low seismic velocity at the base of Earth's mantle, *Nature Geoscience*, *9*(7), 481–489, doi:10.1038/ngeo2733.

Garnero, E. J., and T. Lay (1997), Lateral variations in lowermost mantle shear wave anisotropy beneath the north Pacific and Alaska, *Journal of Geophysical Research: Solid Earth*, *102*(B4), 8121–8135, doi:10.1029/96JB03830.

Garnero, E. J., S. P. Grand, and D. V. Helmberger (1993), Low P-wave velocity at the base of the mantle, *Geophysical Research Letters*, *20*(17), 1843–1846, doi: 10.1029/93GL02009.

Helmberger, D., T. Lay, S. Ni, and M. Gurnis (2005), Deep mantle structure and the post-perovskite phase transition, *Proceedings of the National Academy of Sciences of the United States of America*, *102*(48), 17,257–17,263, doi:10.1073/pnas.0502504102.

Iitaka, T., K. Hirose, K. Kawamura, and M. Murakami (2004), The elasticity of the $MgSiO_3$ post-perovskite phase in the Earth's lowermost mantle, *Nature*, *430*(6998), 442–445, doi:10.1038/nature02702.

Kawai, K., and R. J. Geller (2010), The vertical flow in the lowermost mantle beneath the Pacific from inversion of seismic waveforms for anisotropic structure, *Earth and Planetary Science Letters*, *297*, 190–198.

Kendall, J., and P. Silver (1998), *The Core-Mantle Boundary Region. Geodynamics Series*, vol. 28, chap. Investigating causes of D" anisotropy, American Geophysical Union.

Kendall, J.-M., and P. Silver (1996), Constraints from seismic anisotropy on the nature of the lowermost mantle, *Nature*, *381*(6581), 409–412.

Kennett, B., and E. Engdahl (1991), Traveltimes for global earthquake location and phase identification, *Geophysical Journal International*, *105*(2), 429–465.

Komatitsch, D., and J. Tromp (2002a), Spectral-element simulations of global seismic wave propagation - I. Validation, *Geophysical Journal International*, *149*(2), 390–412.

Komatitsch, D., and J. Tromp (2002b), Spectral-element simulations of global seismic wave propagation - II. Three-dimensional models, oceans, rotation and self-gravitation, *Geophysical Journal International*, *150*(1), 303–318.

Komatitsch, D., and J.-P. Vilotte (1998), The spectral element method: An efficient tool to simulate the seismic response of 2D and 3D geological structures, *Bulletin of the Seismological Society of America*, *88*(2), 368–392.

Komatitsch, D., L. Vinnik, and S. Chevrot (2010), SHdiff-SVdiff splitting in an isotropic Earth, *Journal of Geophysical Research: Solid Earth*, *115*(7).

Kustowski, B., G. Ekström, and A. Dziewonski (2008), Anisotropic shear-wave velocity structure of the earth's mantle: A global model, *Journal of Geophysical Research: Solid Earth*, *113*(6), doi:10.1029/2007JB005169.

Lay, T. (2015), Deep Earth Structure: Lower Mantle and D", in *Treatise on Geophysics, 2nd edition*, vol. 1, edited by G. Schubert, pp. 683–723, Elsevier, Oxford, doi: 10.1016/B978-044452748-6.00022-5.

Lay, T., and D. Helmberger (1983), The shear-wave velocity gradient at the base of the mantle, *Journal of Geophysical Research*, *88*(B10), 8160–8170.

Lekic, V., S. Cottaar, A. Dziewonski, and B. Romanowicz (2012), Cluster analysis of global lower mantle tomography: A new class of structure and implications for chemical heterogeneity, *Earth and Planetary Science Letters*, *357–358*, 68–77, doi: 10.1016/j.epsl.2012.09.014.

Maupin, V. (1994), On the possibility of anisotropy in the D" layer as inferred from the polarization of diffracted S waves, *Physics of the Earth and Planetary Interiors*, *87*(1-2), 1–32, doi:10.1016/0031-9201(94)90019-1.

McNamara, A., P. Van Keken, and S.-I. Karato (2002), Development of anisotropic structure in the Earth's lower mantle by solid-state convection, *Nature*, *416*(6878), 310–314, doi:10.1038/416310a.

Meade, C., P. Silver, and S. Kaneshima (1995), Laboratory and seismological observations of lower mantle isotropy, *Geophysical Research Letters*, *22*(10), 1293–1296.

Montagner, J.-P., and B. Kennett (1996), How to reconcile body-wave and normal-mode reference earth models, *Geophysical Journal International*, *125*(1), 229–248.

Murakami, M., K. Hirose, K. Kawamura, N. Sata, and Y. Ohishi (2004), Post-Perovskite Phase Transition in $MgSiO_3$, *Science*, *304*(5672), 855–858, doi: 10.1126/science.1095932, cited By 702.

Nowacki, A., J. Wookey, and J.-M. Kendall (2011), New advances in using seismic anisotropy, mineral physics and geodynamics to understand deformation in the lowermost mantle, *Journal of Geodynamics*, *52*(3-4), 205–228.

Oganov, A., R. Martonak, A. Laio, P. Raiteri, and M. Parrinello (2005), Anisotropy of Earth's D" layer and stacking faults in the $MgSiO_3$ post-perovskite phase, *Nature*, *438*(7071), 1142–1144, doi:10.1038/nature04439.

Parisi, L., and A. M. G. Ferreira (2016), Empirical assessment of the validity limits of the surface wave full ray theory using realistic 3-D Earth models, *Geophysical Journal International*, *205*(1), 146–159, doi:10.1093/gji/ggw005.

Parisi, L., A. M. G. Ferreira, and Y. Capdeville (2015), Validity domain of the Born approximation for seismic waveform modelling in realistic 3-D Earth structure, *Geophysical Journal International*, *200*, 908–914, doi:10.1093/gji/ggu446.

Pulliam, J., and M. Sen (1998), Seismic anisotropy in the core-mantle transition zone, *Geophysical Journal International*, *135*(1), 113–128, doi:10.1046/j.1365-246X.1998.00612.x.

Ritsema, J. (2000), Evidence for shear velocity anisotropy in the lowermost mantle beneath the Indian Ocean, *Geophysical Research Letters*, *27*(7), 1041–1044.

Ritsema, J., E. Garnero, and T. Lay (1997), A strongly negative shear velocity gradient and lateral variability in the lowermost mantle beneath the pacific, *Journal of Geophysical Research B: Solid Earth*, *102*(B9), 20,395–20,411.

Ritsema, J., T. Lay, E. Garnero, and H. Benz (1998), Seismic anisotropy in the lowermost mantle beneath the Pacific, *Geophysical Research Letters*, *25*(8), 1229–1232.

Ritsema, J., A. Deuss, H. Van Heijst, and J. Woodhouse (2011), S40RTS: A degree-40 shear-velocity model for the mantle from new Rayleigh wave dispersion, teleseismic traveltime and normal-mode splitting function measurements, *Geophysical Journal International*, *184*(3), 1223–1236, doi:10.1111/j.1365-246X.2010.04884.x.

Sun, D., D. Helmberger, M. Miller, and J. Jackson (2016), Major disruption of D" beneath Alaska, *Journal of Geophysical Research: Solid Earth*, *121*(5), 3534–3556, doi: 10.1002/2015JB012534.

Thomas, C., and J.-M. Kendall (2002), The lowermost mantle beneath northern Asia - II. Evidence for lower-mantle anisotropy, *Geophysical Journal International*, *151*(1), 296–308, doi:10.1046/j.1365-246X.2002.01760.x.

Thorne, M., E. Garnero, G. Jahnke, H. Igel, and A. McNamara (2013), Mega ultra low velocity zone and mantle flow, *Earth and Planetary Science Letters*, *364*, 59–67, doi: 10.1016/j.epsl.2012.12.034.

Vinnik, L., B. Romanowicz, Y. Le Stunff, and L. Makeyeva (1995), Seismic anisotropy in the D" layer, *Geophysical Research Letters*, *22*(13), 1657–1660, doi: 10.1029/95GL01327.

Vinnik, L., L. Breger, and B. Romanowicz (1998), Anisotropic structures at the base of the Earth's mantle, *Nature*, *393*(6685), 564–567, doi:10.1038/31208.

Wysession, M., T. Lay, J. Revenaugh, Q. Williams, E. Garnero, R. Jeanloz, and L. Kellogg (1998), The D" discontinuity and its implications, in *The Core-Mantle Boundary Region. Geodynamics Series, 28*, edited by W. M. K. E. B. B. Gurnis, M., pp. 273–298, American Geophysical Union, Washington, D.C., USA.

Wysession, M. E., A. Langenhorst, M. J. Fouch, K. M. Fischer, G. I. Al-Eqabi, P. J. Shore, and T. J. Clarke (1999), Lateral variations in compressional/shear velocities at the base of the mantle, *Science*, *284*(5411).

Yao, Y., S. Whittaker, and M. S. Thorne (2015), D” discontinuity structure beneath the North Atlantic from Scd observations, *Geophysical Research Letters*, *42*(10), 3793–3801, doi:10.1002/2015GL063989.

Young, C., and T. Lay (1987a), Evidence for a shear velocity discontinuity in the lower mantle beneath India and the Indian Ocean, *Physics of the Earth and Planetary Interiors*, *49*(1–2), 37–53, doi:10.1016/0031-9201(87)90131-2.

Young, C., and T. Lay (1987b), The core–mantle boundary, in *Annual Review of Earth and Planetary Sciences*, vol. 15, pp. 25–46.

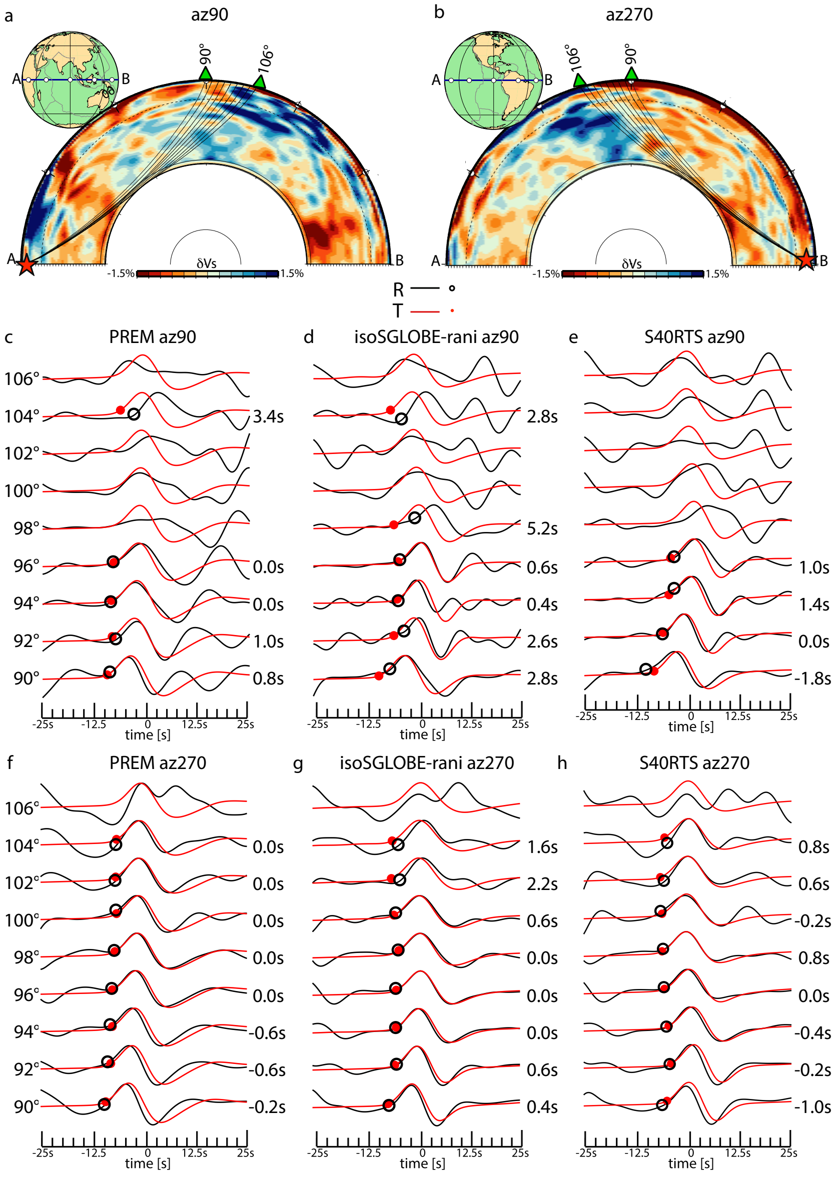

Figure 8. Effects of 3-D Earth structure on the shape of S waveforms. **a)** Rays in PREM are shown for S phases recorded from 90° to 106° for the same source as in Figure 2 but at source depth of 604 km. The stations are at an azimuth of 90°. The source location is represented by the red star and the receivers are represented by green triangles. Vs perturbations of the isotropic part of the SGLOBE-rani tomographic model with respect to the isotropic PREM are shown in the background of the cross-sections. **b)** As in a) but for an azimuth of 270°. **c)** Velocity waveforms calculated for the source-receiver geometry in a) and 1-D Earth model PREM (isotropic). The epicentral distance range is shown on the left of the waveforms. SH (black circles) and SV (red dots) onsets are marked on the waveforms. The measured apparent splitting is indicated on the right. Every waveform is normalised with respect to its own maximum amplitude. **d)** As in b) but for the isotropic part of 3-D Earth model SGLOBE-rani. **e)** As in b) but for the 3-D Earth model S40RTS. **f)** As in c) but for the geometry in b). **g)** As in f) but for the isotropic part of 3-D Earth model SGLOBE-rani. **h)** As in f) but for the 3-D Earth model S40RTS.

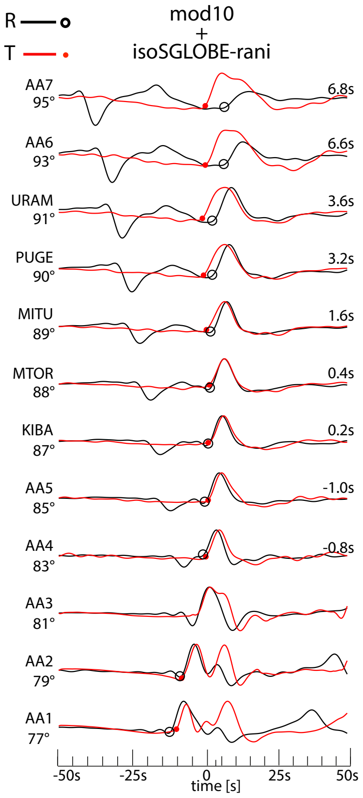

Figure 9. Effects of 3-D Earth's structure on S waveforms. Waveforms calculated for the isotropic part of the SGLOBE-rani model, superimposed to the 1-D Earth model mod10. PREM's attenuation is included. On the left of the waveforms, the names of the stations and the epicentral distances are reported. SV (black circles) and SH (red dots) onsets are marked on the waveforms. The apparent splitting is reported on the right of the waveforms. The source-receiver geometry is shown in Figure 4. Every waveform is normalized with respect to its own maximum amplitude.

Figure 1.

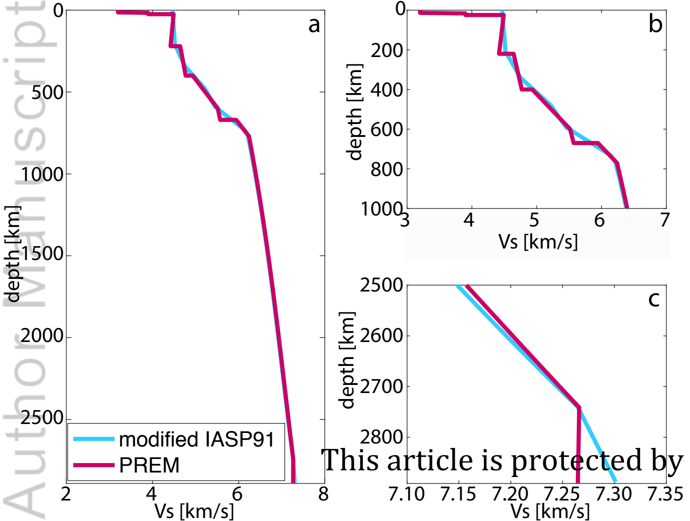
a
0
500
1000
1500
2000
2500
depth [km]
modified IASP91
PREM
2
4
6
8
Vs [km/s]
b
0
200
400
600
800
1000
depth [km]
3
4
5
6
7
Vs [km/s]
c
2500
2600
2700
2800
depth [km]
7.10
7.15
7.20
7.25
7.30
7.35
Vs [km/s]

Figure 2.

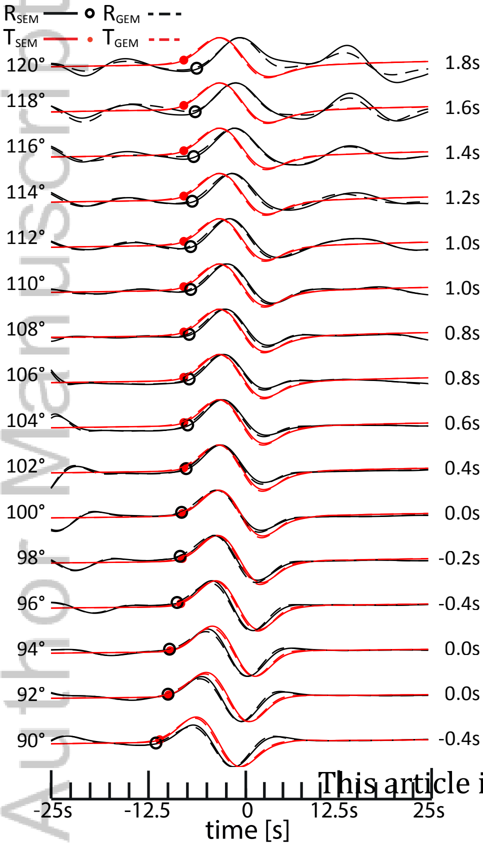
R_SEM
R_GEM
T_SEM
T_GEM
120° 1.8s
118° 1.6s
116° 1.4s
114° 1.2s
112° 1.0s
110° 1.0s
108° 0.8s
106° 0.8s
104° 0.6s
102° 0.4s
100° 0.0s
98° -0.2s
96° -0.4s
94° 0.0s
92° 0.0s
90° -0.4s
-25s
-12.5
0
12.5s
25s
time [s]

Figure 3.

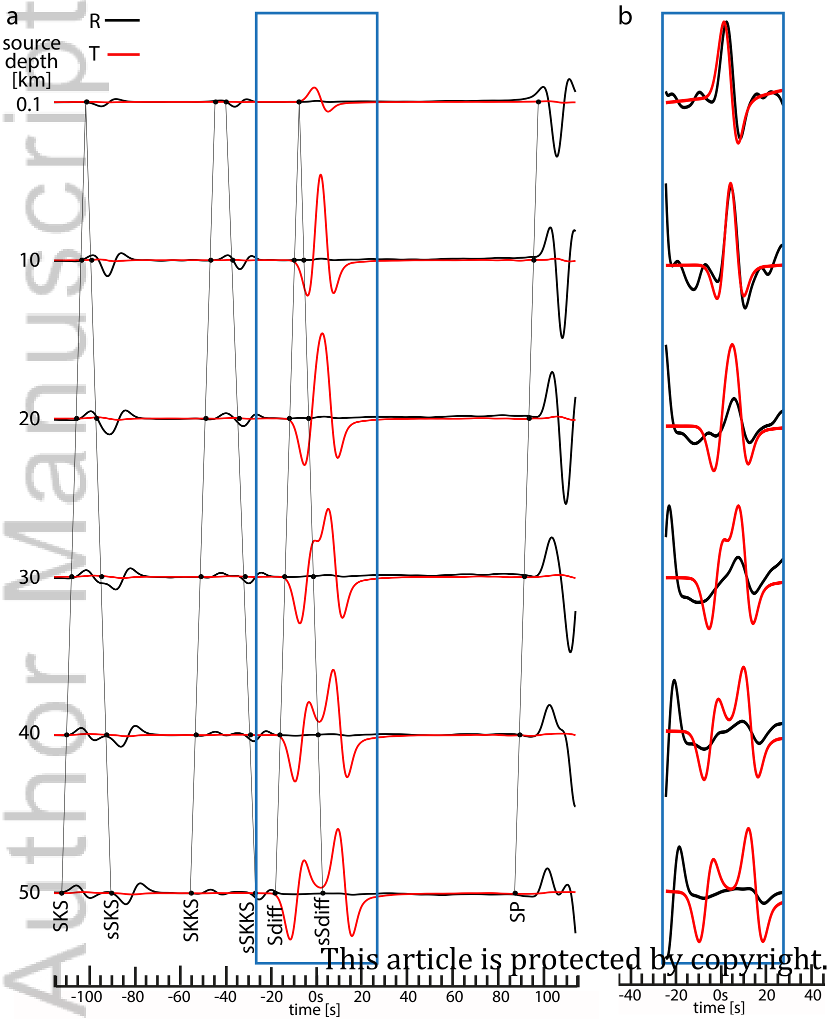
a
source depth [km]
R
T
0.1
10
20
30
40
50
SKS
sSKS
SKKS
sSKKS
Sdiff
sSdiff
SP
-100
-80
-60
-40
-20
0s
20
40
60
80
100
time [s]
b
-40
-20
0s
20
40
time [s]

Figure 4.

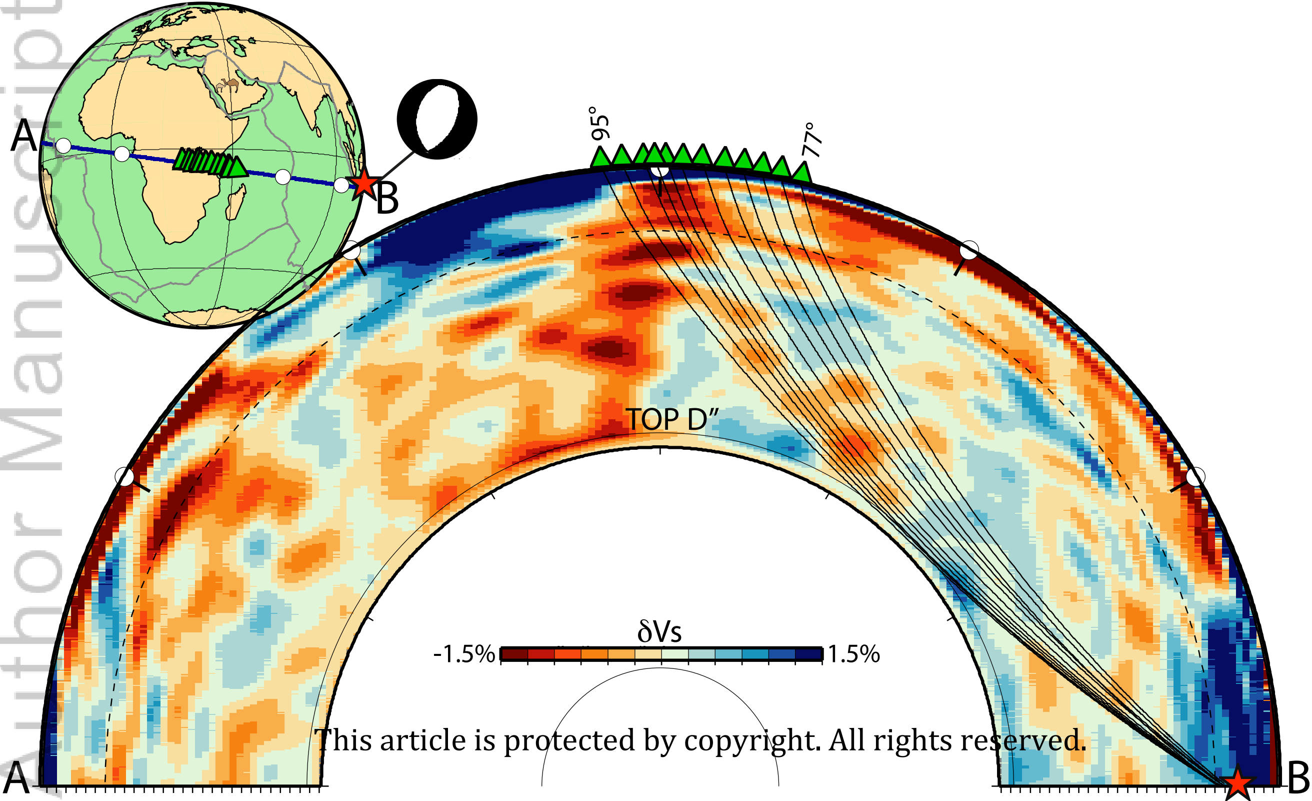
A
B
95°
77°
TOP D"
δVs
-1.5%
1.5%
A
B

Figure 5.

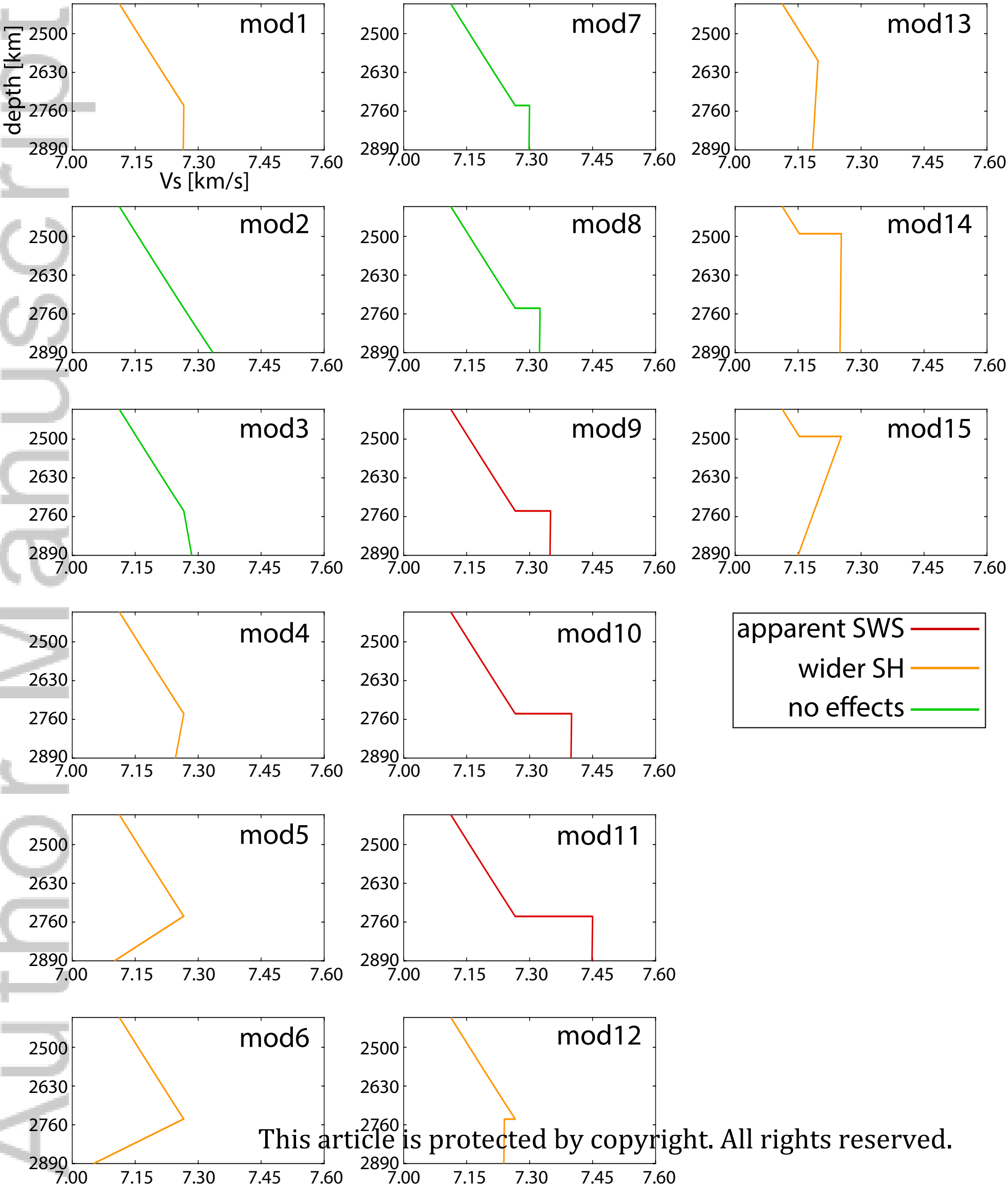
mod1
mod2
mod3
mod4
mod5
mod6
mod7
mod8
mod9
mod10
mod11
mod12
mod13
mod14
mod15
depth [km]
2500
2630
2760
2890
7.00
7.15
7.30
7.45
7.60
Vs [km/s]
apparent SWS
wider SH
no effects

Figure 6.

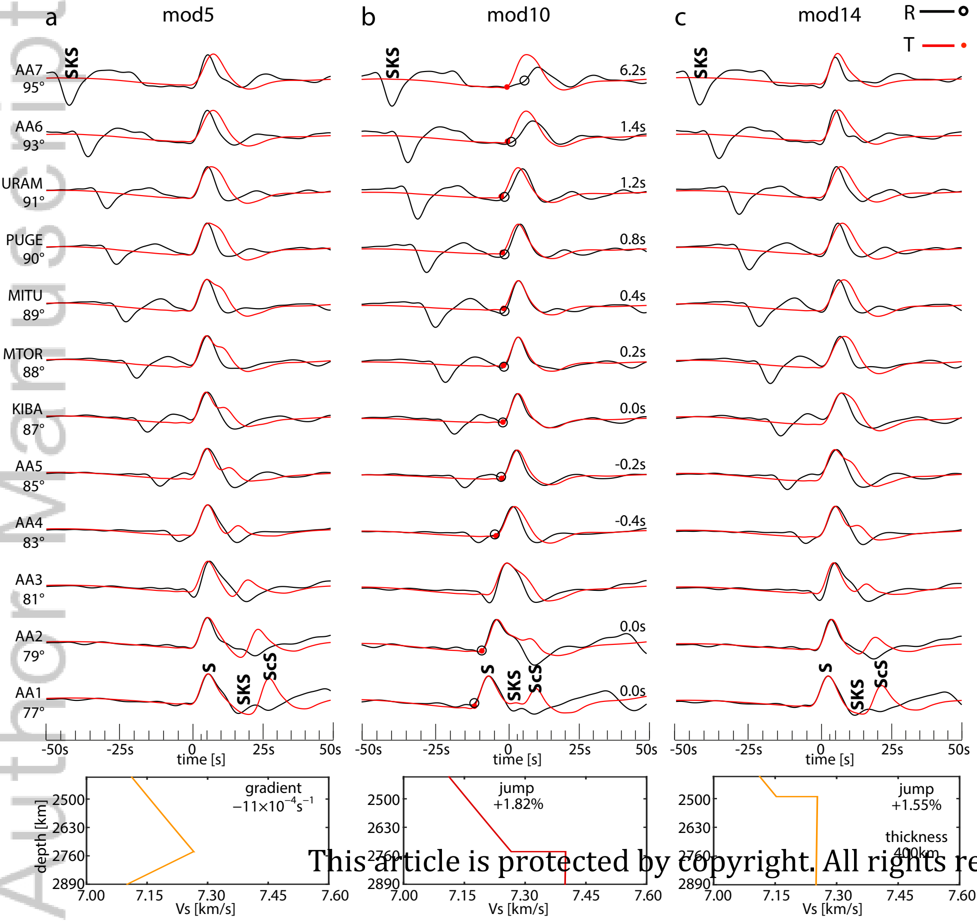
a
mod5
b
mod10
c
mod14
R
T
SKS
AA7 95°
AA6 93°
URAM 91°
PUGE 90°
MITU 89°
MTOR 88°
KIBA 87°
AA5 85°
AA4 83°
AA3 81°
AA2 79°
AA1 77°
6.2s
1.4s
1.2s
0.8s
0.4s
0.2s
0.0s
-0.2s
-0.4s
0.0s
0.0s
S
SKS
ScS
-50s
-25s
0
25s
50s
time [s]
depth [km]
2500
2630
2760
2890
7.00
7.15
7.30
7.45
7.60
Vs [km/s]
gradient
$-11\times10^{-4}s^{-1}$
jump
+1.82%
jump
+1.55%
thickness
400km

Figure 7.

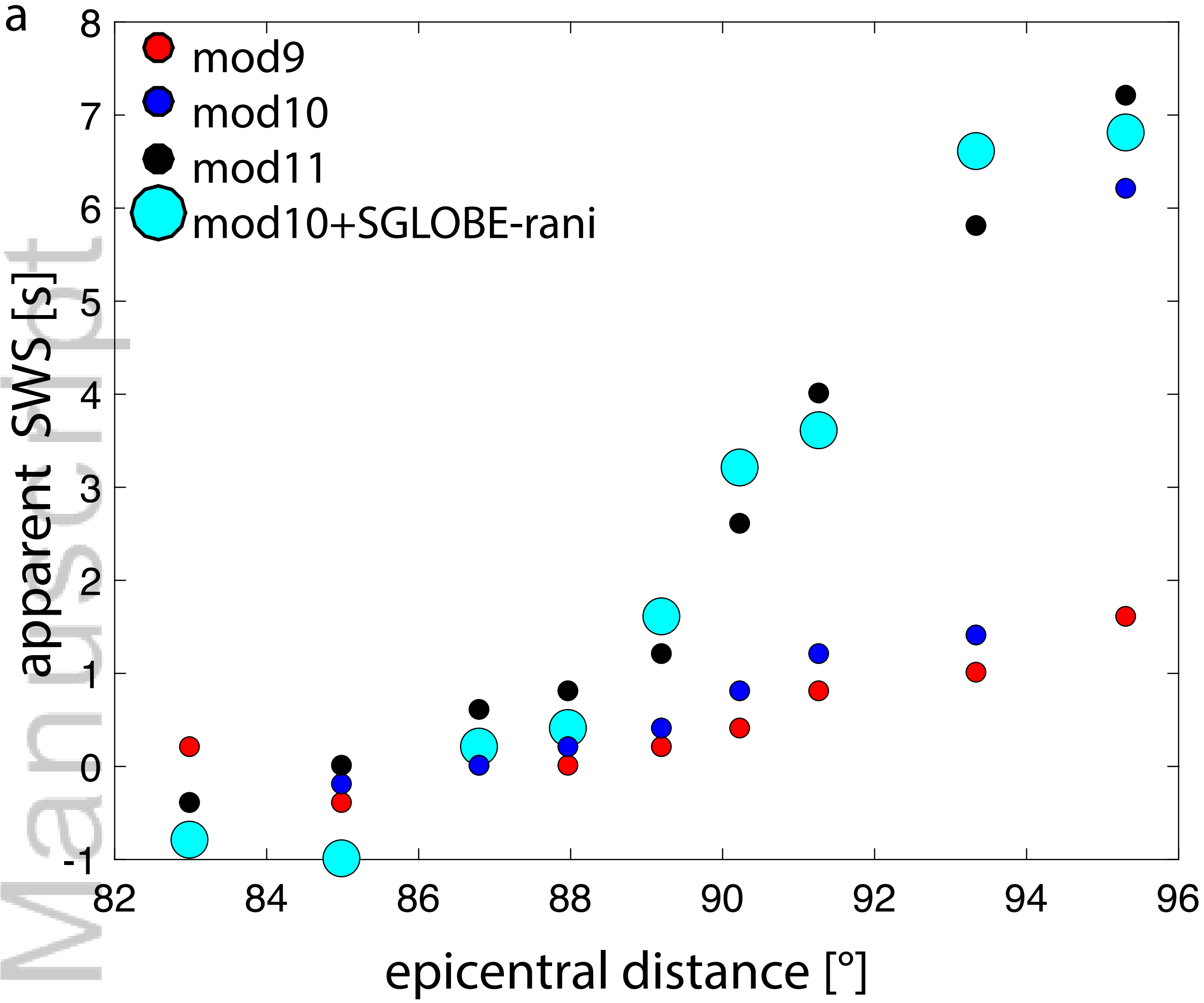

b

	Distance	SWS
South East Pacific	~90°	~-2s -- ~+2s
Ford at al., 2006	~95°	~-4s -- ~+4s
Caribbean	~90°	~+2s
Kendall and Silver, 1996	~92°	~+5s
Alaska	~90°	0 -- ~+1.5s

Figure 8.

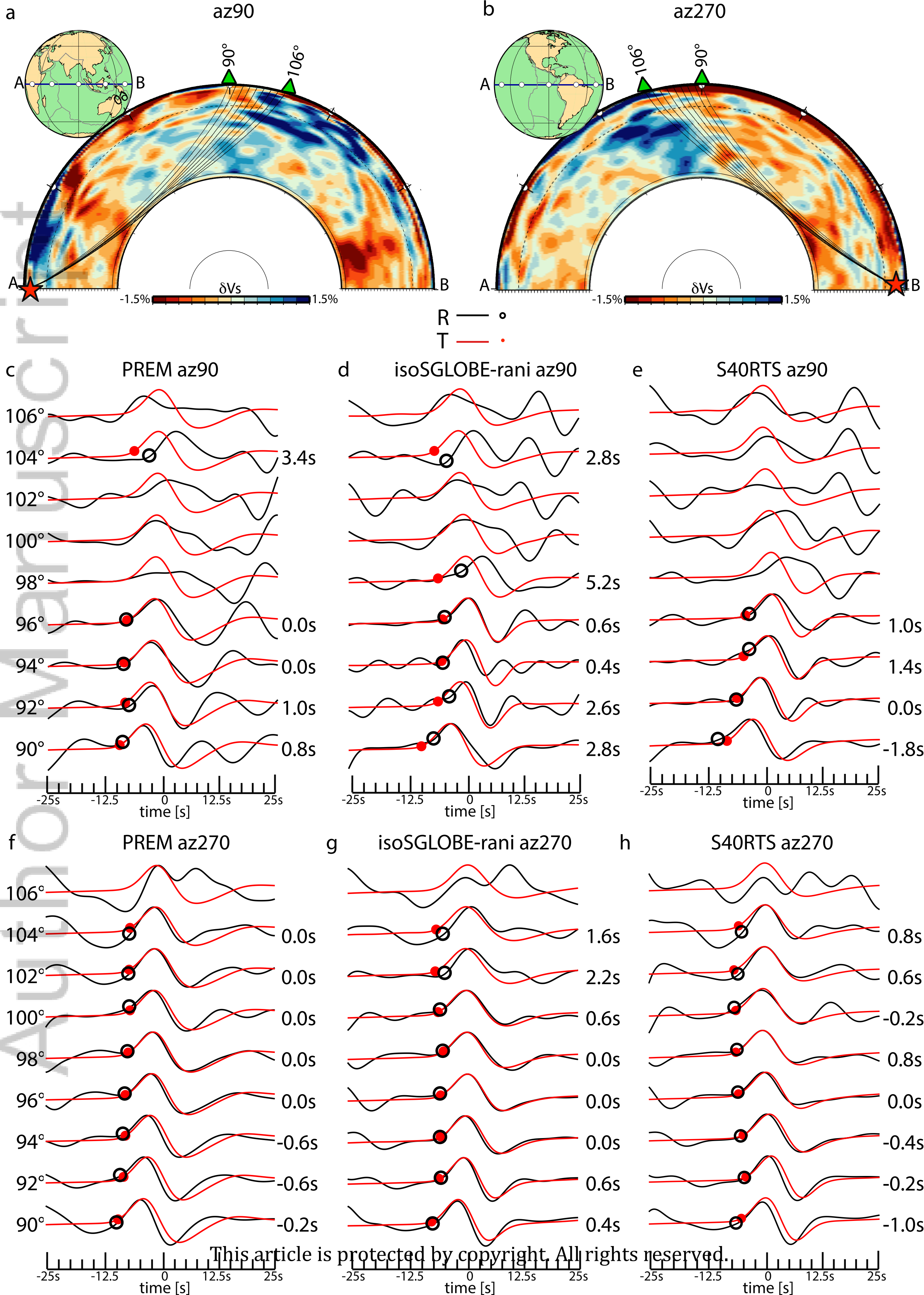
a
az90
b
az270
A
B
90°
106°
δVs
-1.5%
1.5%
R
T
c
PREM az90
d
isoSGLOBE-rani az90
e
S40RTS az90
106°
104°
102°
100°
98°
96°
94°
92°
90°
3.4s
0.0s
0.0s
1.0s
0.8s
2.8s
5.2s
0.6s
0.4s
2.6s
2.8s
1.0s
1.4s
0.0s
-1.8s
-25s
-12.5
0
12.5s
25s
time [s]
f
PREM az270
g
isoSGLOBE-rani az270
h
S40RTS az270
0.0s
0.0s
0.0s
0.0s
0.0s
-0.6s
-0.6s
-0.2s
1.6s
2.2s
0.6s
0.0s
0.0s
0.0s
0.6s
0.4s
0.8s
0.6s
-0.2s
0.8s
0.0s
-0.4s
-0.2s
-1.0s

Figure 9.

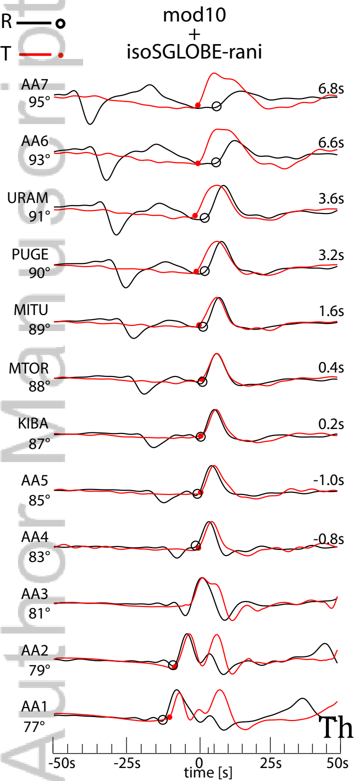
R
T
mod10
+
isoSGLOBE-rani
AA7
95°
6.8s
AA6
93°
6.6s
URAM
91°
3.6s
PUGE
90°
3.2s
MITU
89°
1.6s
MTOR
88°
0.4s
KIBA
87°
0.2s
AA5
85°
-1.0s
AA4
83°
-0.8s
AA3
81°
AA2
79°
AA1
77°
-50s
-25s
0
25s
50s
time [s]

Th

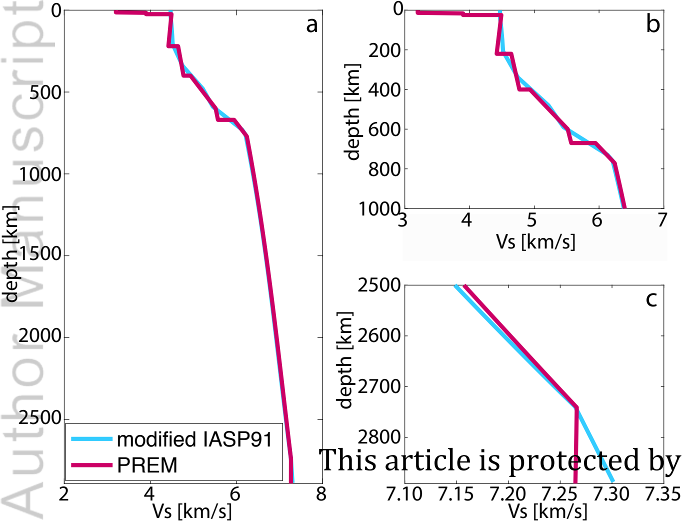
0
500
1000
1500
2000
2500
depth [km]
a
2
4
6
8
Vs [km/s]
modified IASP91
PREM
0
200
400
600
800
1000
depth [km]
b
3
4
5
6
7
Vs [km/s]
2500
2600
2700
2800
depth [km]
c
7.10
7.15
7.20
7.25
7.30
7.35
Vs [km/s]

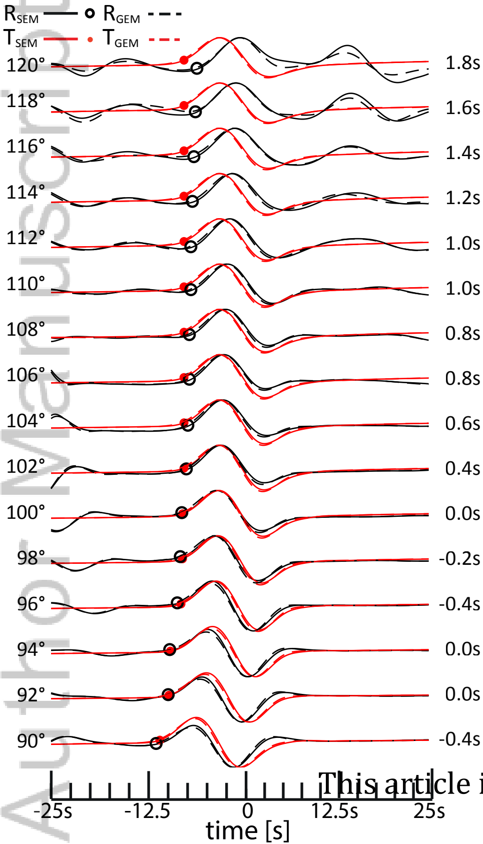
R_{SEM}
R_{GEM}
T_{SEM}
T_{GEM}
120°
118°
116°
114°
112°
110°
108°
106°
104°
102°
100°
98°
96°
94°
92°
90°
1.8s
1.6s
1.4s
1.2s
1.0s
1.0s
0.8s
0.8s
0.6s
0.4s
0.0s
-0.2s
-0.4s
0.0s
0.0s
-0.4s
-25s
-12.5
0
12.5s
25s
time [s]

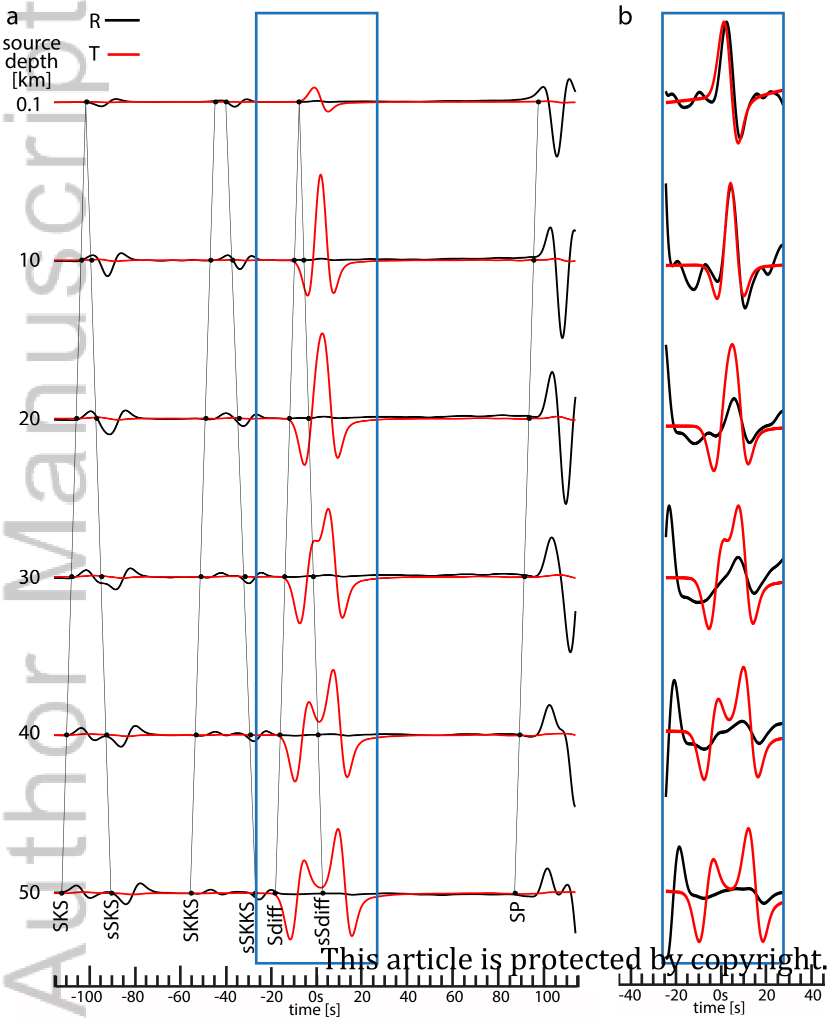
a
R
T
source depth [km]
0.1
10
20
30
40
50
SKS
sSKS
SKKS
sSKKS
Sdiff
sSdiff
SP
-100
-80
-60
-40
-20
0s
20
40
60
80
100
time [s]
b
-40
-20
0s
20
40
time [s]

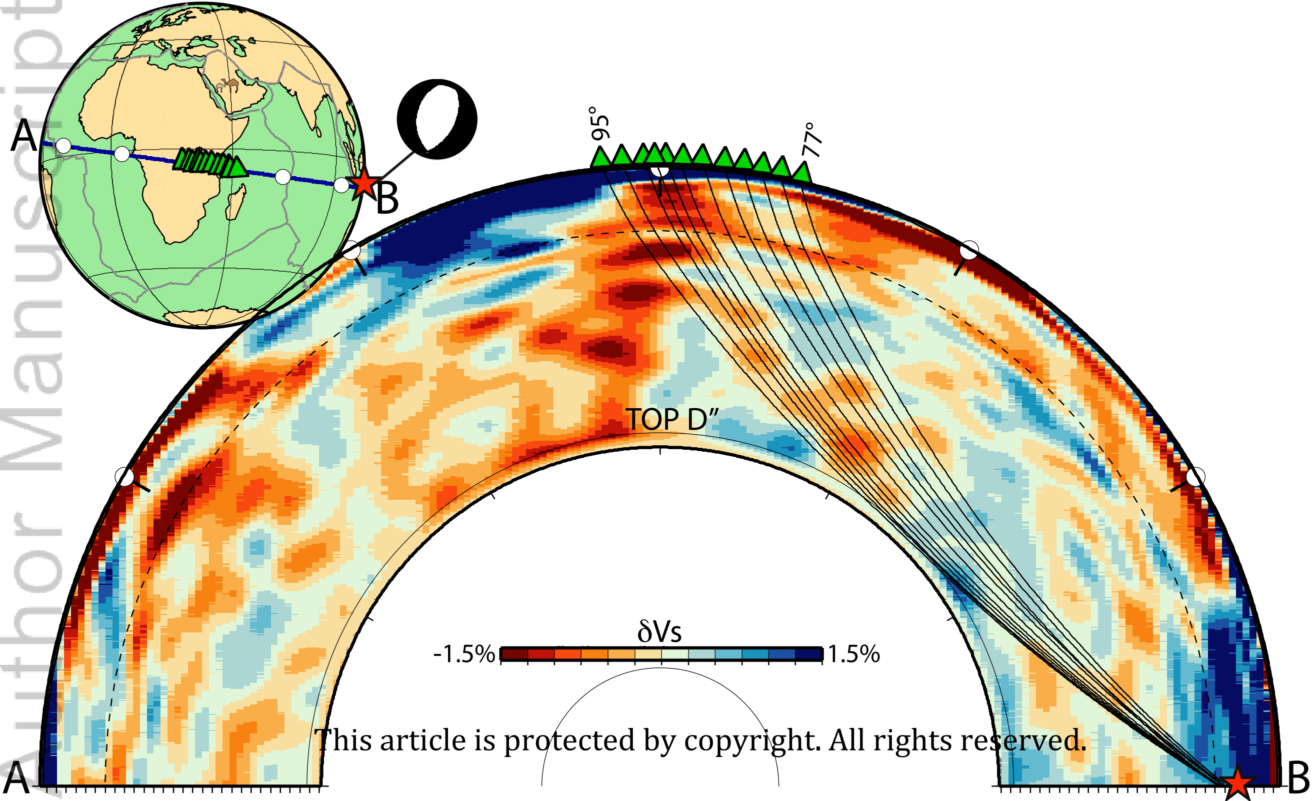
A
B
95°
77°
TOP D"
δVs
-1.5%
1.5%
A
B

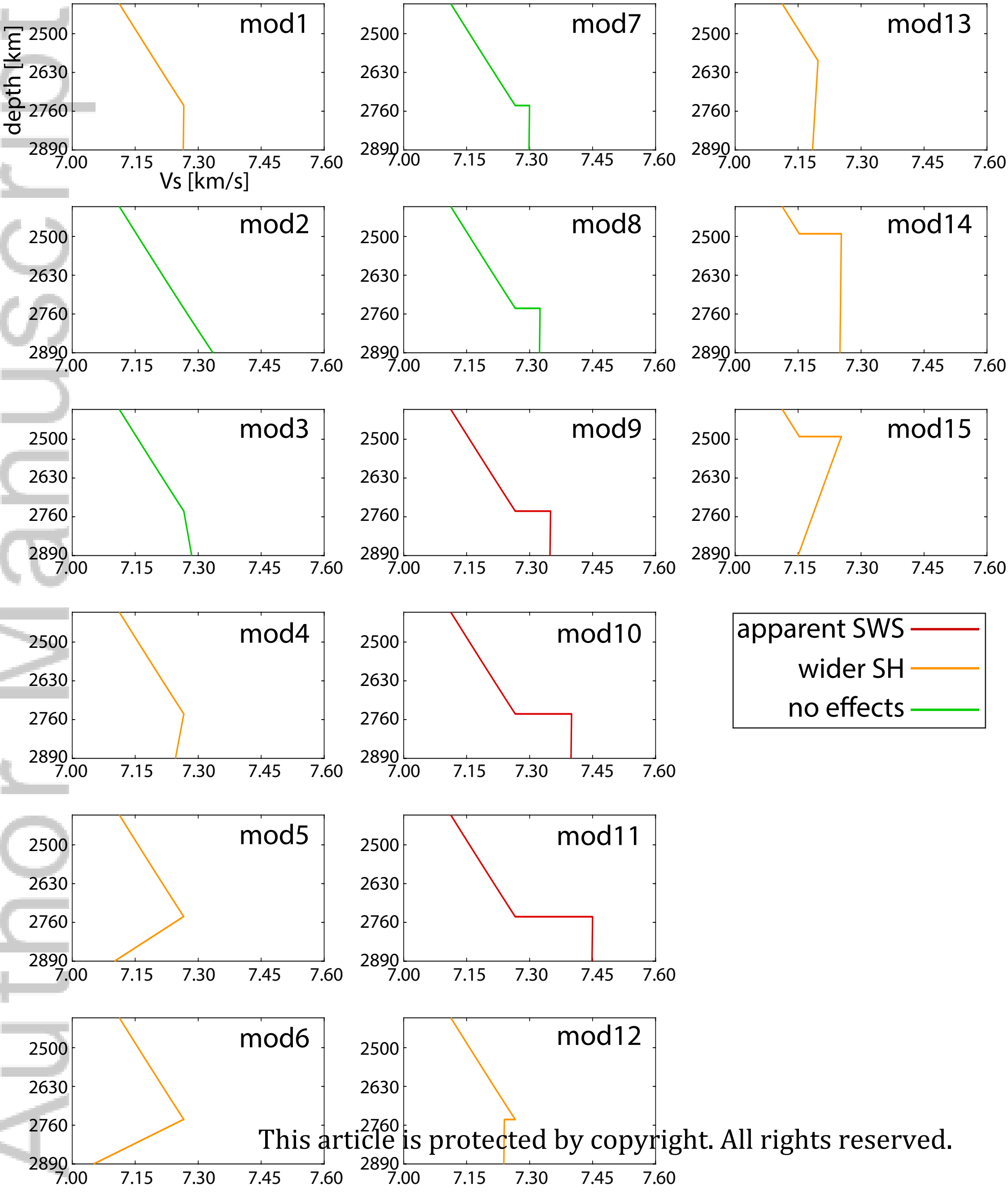
mod1
mod2
mod3
mod4
mod5
mod6
mod7
mod8
mod9
mod10
mod11
mod12
mod13
mod14
mod15
depth [km]
2500
2630
2760
2890
7.00
7.15
7.30
7.45
7.60
Vs [km/s]
apparent SWS
wider SH
no effects

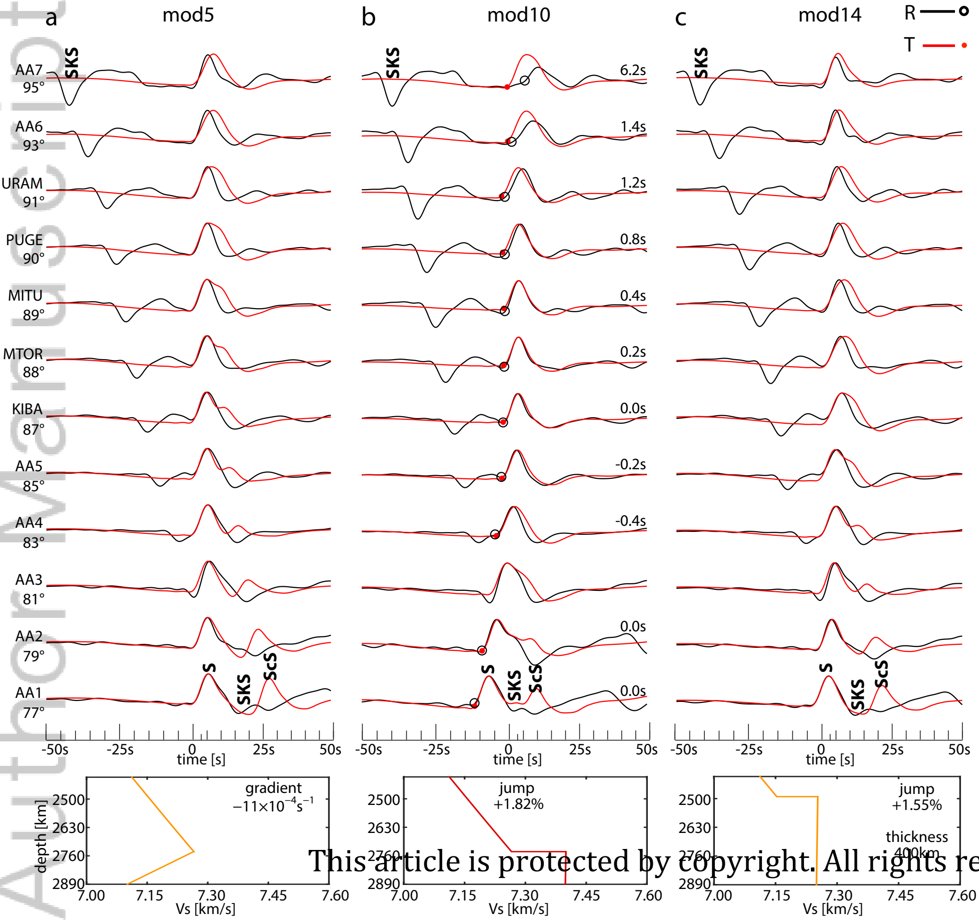
a
mod5
b
mod10
c
mod14
R
T
SKS
AA7
95°
AA6
93°
URAM
91°
PUGE
90°
MITU
89°
MTOR
88°
KIBA
87°
AA5
85°
AA4
83°
AA3
81°
AA2
79°
AA1
77°
S
SKS
ScS
6.2s
1.4s
1.2s
0.8s
0.4s
0.2s
0.0s
-0.2s
-0.4s
0.0s
0.0s
-50s
-25s
0
25s
50s
time [s]
gradient
−11×10^{-4}s^{-1}
jump
+1.82%
jump
+1.55%
thickness
400km
depth [km]
2500
2630
2760
2890
7.00
7.15
7.30
7.45
7.60
Vs [km/s]

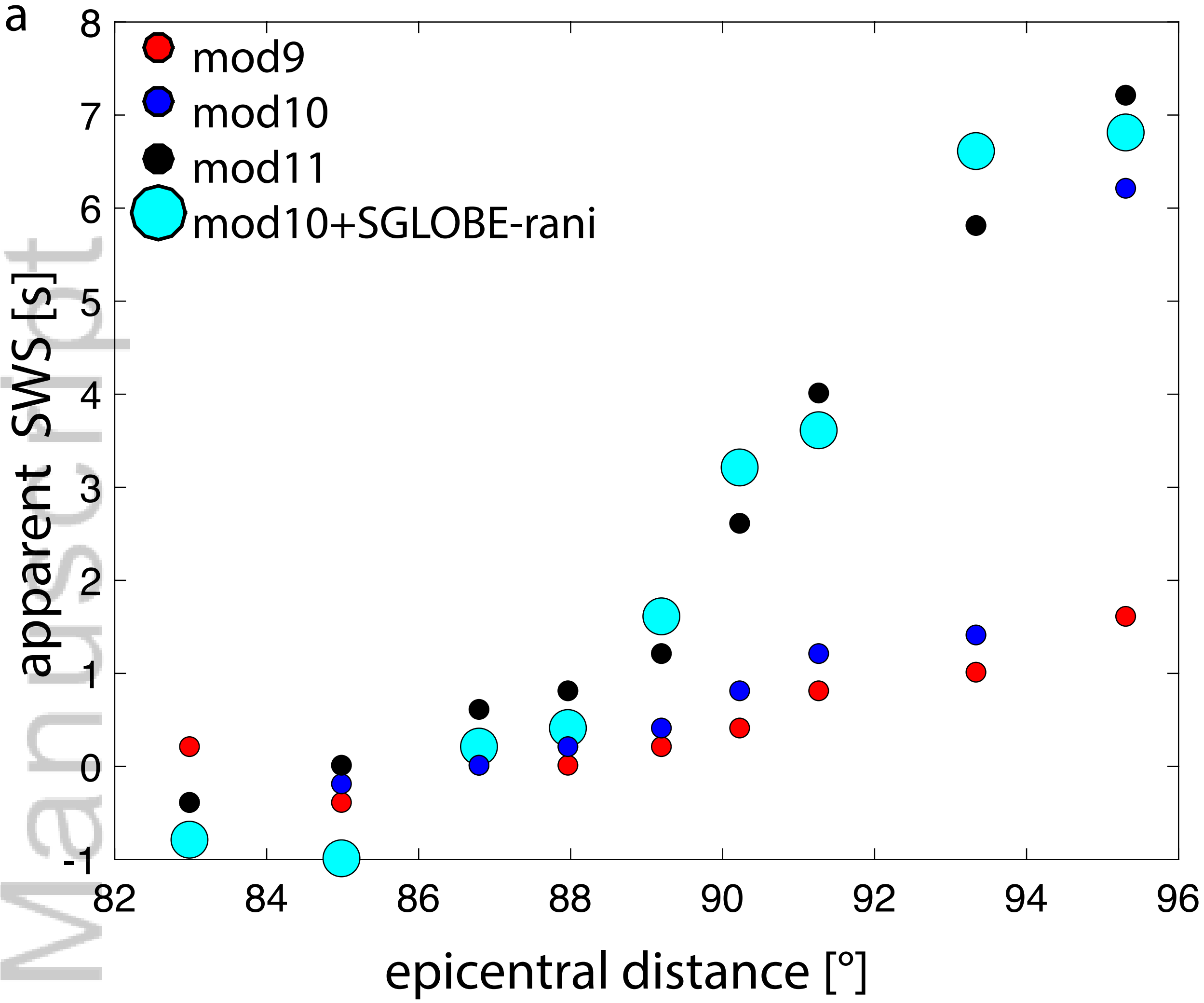

b

	Distance	SWS
South East Pacific	~90°	~-2s -- ~+2s
Ford at al., 2006	~95°	~-4s -- ~+4s
Caribbean	~90°	~+2s
Kendall and Silver, 1996	~92°	~+5s
Alaska	~90°	0 -- ~+1.5s

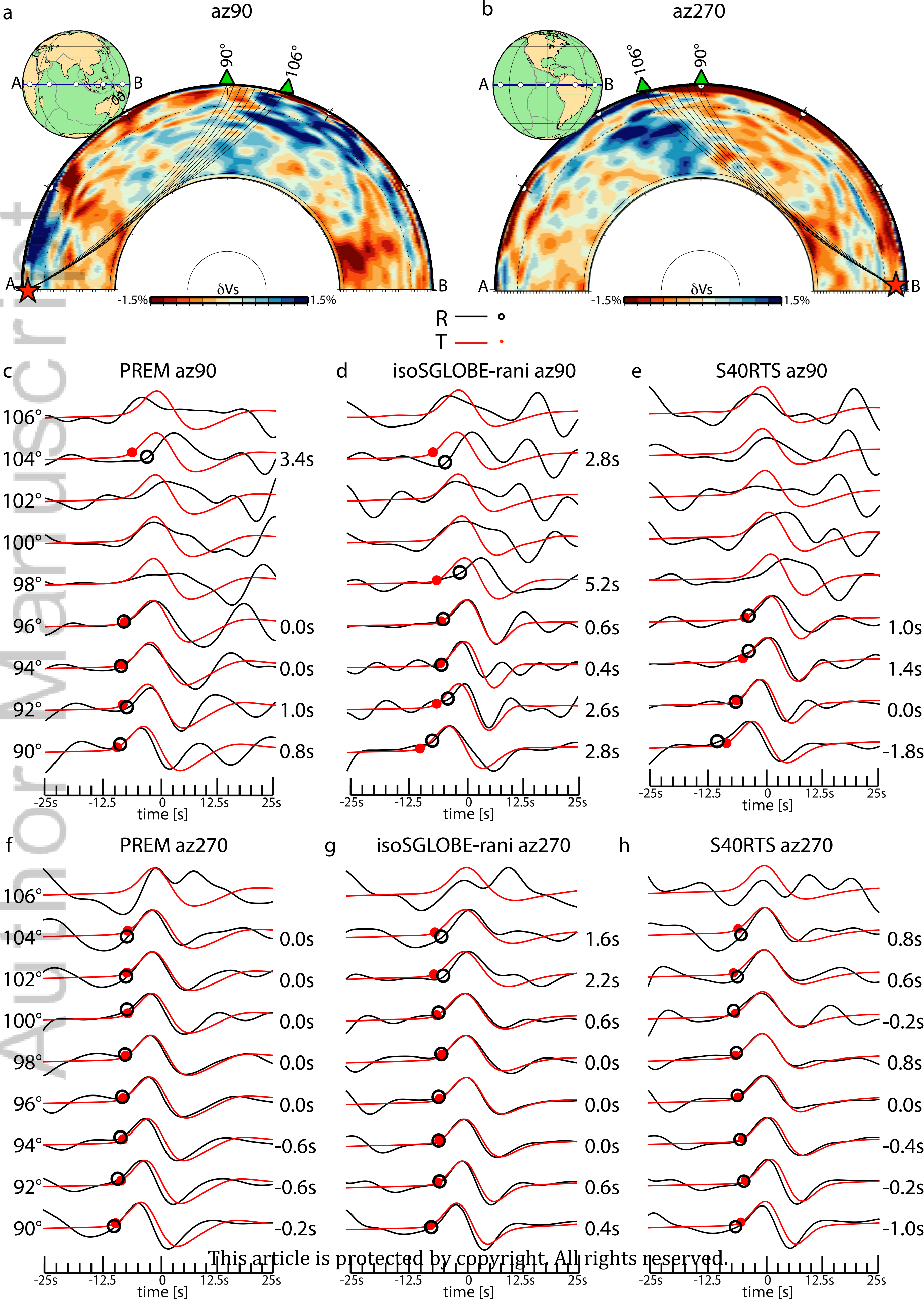
a
az90
A
B
90°
106°
δVs
-1.5%
1.5%
b
az270
106°
90°
R
T
c
PREM az90
d
isoSGLOBE-rani az90
e
S40RTS az90
106°
104°
102°
100°
98°
96°
94°
92°
90°
3.4s
0.0s
0.0s
1.0s
0.8s
2.8s
5.2s
0.6s
0.4s
2.6s
2.8s
1.0s
1.4s
0.0s
-1.8s
-25s
-12.5
0
12.5s
25s
time [s]
f
PREM az270
g
isoSGLOBE-rani az270
h
S40RTS az270
0.0s
0.0s
0.0s
0.0s
0.0s
-0.6s
-0.6s
-0.2s
1.6s
2.2s
0.6s
0.0s
0.0s
0.0s
0.6s
0.4s
0.8s
0.6s
-0.2s
0.8s
0.0s
-0.4s
-0.2s
-1.0s

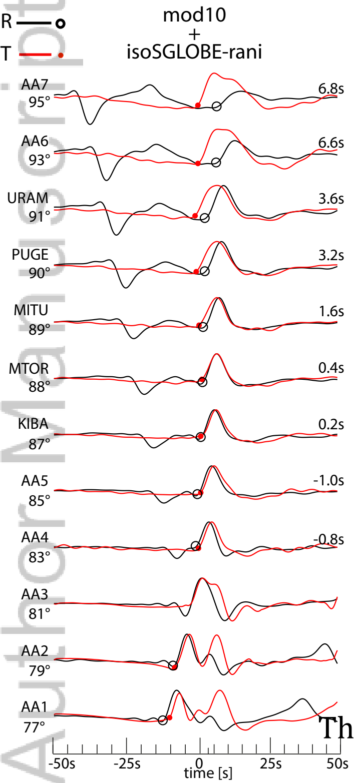
R
T
mod10
+
isoSGLOBE-rani
AA7
95°
6.8s
AA6
93°
6.6s
URAM
91°
3.6s
PUGE
90°
3.2s
MITU
89°
1.6s
MTOR
88°
0.4s
KIBA
87°
0.2s
AA5
85°
-1.0s
AA4
83°
-0.8s
AA3
81°
AA2
79°
AA1
77°
-50s
-25s
0
25s
50s
time [s]

Th